INTERNATIONAL JOURNAL FOR NUMERICAL METHODS IN ENGINEERING
Int. J. Numer. Meth. Engng 2010; **82**:329–358
Published online 9 November 2009 in Wiley InterScience (www.interscience.wiley.com). DOI: 10.1002/nme.2767

Transient three-dimensional domain decomposition problems: Frame-indifferent mortar constraints and conserving integration

Christian Hesch*, †, ‡ and Peter Betsch

Department of Mechanical Engineering, University of Siegen, Germany

SUMMARY

The present work deals with transient large-deformation domain decomposition problems. The tying of dissimilar meshed grids is performed by applying the mortar method. In this connection, a reformulation of the original linear mortar constraints is proposed, which retains frame-indifference for arbitrary discretizations of the interface. Furthermore, a specific coordinate augmentation technique is proposed to make possible the design of an energy–momentum scheme. Numerical examples demonstrate the robustness and enhanced numerical stability of the newly developed energy–momentum scheme for three-dimensional problems. Copyright © 2009 John Wiley & Sons, Ltd.

Received 28 April 2009; Revised 3 September 2009; Accepted 6 September 2009

KEY WORDS: domain decomposition; mortar methods; energy–momentum

1. INTRODUCTION

Domain decomposition methods arise within the context of many different applications. A lot of these applications deal with multiphysics and similar problems (see Quarterone and Valli [1] and the references therein). Furthermore, domain decomposition methods are the most common paradigm for large-scale simulation on parallel computers. The research in this area can be traced back to the work published by Schwarz [2] in 1870. Parallel to the development of high-performance computers, this topic gained more attention by the research community since the beginning of the 1980s (see Hackbusch [3]). Especially in the context of iterative solvers, highly advanced techniques have been developed in recent years ([4], see also the lecture notes in [5, 6]).

Coupling of non-conforming meshes via the so-called node-to-segment (NTS) method has been proposed originally for contact problems by Hallquist *et al.* [7]. For a survey of actual developments in the field of contact methods, we refer to the books by Laursen [8] and Wriggers [9]. The collocation-type NTS method does not pass the patch test and exhibits poor convergence properties.

*Correspondence to: Christian Hesch, Department of Mechanical Engineering, University of Siegen, Germany.
†E-mail: hesch@imr.mb.uni-siegen.de
‡Chair of Computational Mechanics.

In particular, the local errors at the contact region do not necessarily diminish with mesh refinement (see El-Abassi and Bathe [10]).

In the early 90s of the past century, a variationally consistent mesh-tying method (the so-called mortar method) has been developed by Bernadi *et al.* [11, 12]. The extension of this method to linear elasticity problems can be found in Krause and Wohlmuth [13]. A similar method for connecting dissimilar three-dimensional finite element meshes in the context of linear elasticity problems has been presented by Dohrmann *et al.* [14], see also Heinstein and Laursen [15]. An extension of the mortar mesh-tying method to three-dimensional non-linear elasticity has been proposed by Puso [16]. The application of the mortar method to large-deformation contact problems can be found, for example, in Puso *et al.* [17], Yang *et al.* [18] and Yang and Laursen [19]. A comparison between the NTS and the mortar method in the context of two-dimensional large-deformation contact problems has been presented by Hesch and Betsch [20].

It is now well established that energy–momentum conserving time-stepping schemes (see e.g. Gonzalez [21, 22] and Betsch and Steinman [23, 24]) and energy-decaying variants thereof (see e.g. Armero and Romero [25, 26]) provide enhanced numerical stability for applications in non-linear structural dynamics and elastodynamics. Energy-conserving time-stepping schemes for large-deformation contact problems have been developed within the framework of the NTS method, see, for example Laursen and Chawla [27], Armero and Petöcz [28], Laursen and Love [29], Hauret and Le Tallec [30], Haikal and Hjelmstad [31] and Betsch and Hesch [32]. For planar large-deformation contact problems, a mortar-based energy–momentum scheme has been recently proposed by Hesch and Betsch [33].

The original formulation of the mortar method for large-deformation domain decomposition yields linear mesh-tying constraints, which generally fail to be invariant under rigid body rotations. To restore frame-invariance of the mortar constraints, Puso [16] proposed a mesh initialization procedure for repositioning the non-mortar nodes in the reference configuration. In the present work, we present a reformulation of the mortar mesh-tying constraints that preserves the crucial property of frame-invariance for arbitrarily meshed interfaces. The frame-indifferent reformulation of the mortar constraints then provides the foundation for the development of an energy–momentum scheme.

An outline of the present work is as follows. Section 2 gives a short introduction to the continuous problem under consideration. Section 3 provides a finite element discretization of the large-deformation problem including the mesh-tying interface. In Section 4 we utilize the NTS method to develop a frame-indifferent formulation of the corresponding mesh-tying constraints. In addition to that, a special coordinate augmentation technique is developed that facilitates the design of an energy–momentum scheme. In Section 5 we extend these concepts to the mortar method. The equations of motion of the finite-dimensional constrained mechanical system under consideration along with the conserving discretization in time are dealt with in Section 6. Representative numerical examples are presented in Section 7. Eventually, conclusions are drawn in Section 8.

2. LARGE-DEFORMATION FORMULATION

This section provides a short outline of the mechanical problem under consideration. For that purpose, Figure 1 shows a schematic illustration of a typical body, subdivided into two parts, which are both tied together on the interface Γ_d. It is assumed that there exists for each part (i) a mapping $\boldsymbol{\varphi}^{(i)}(\boldsymbol{X}^{(i)}, t)$, characterizing the current position at time t of a material point $\boldsymbol{X}^{(i)}$ in

DOI: 10.1002/nme

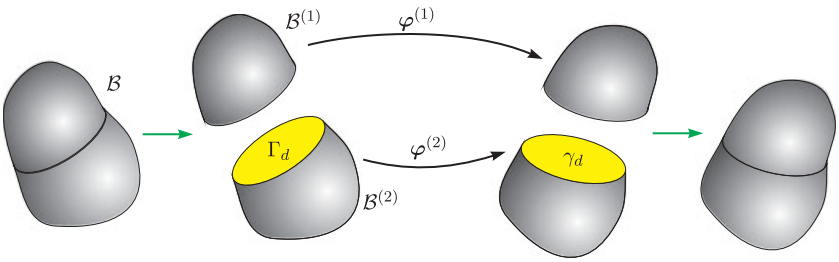

Figure 1. Typical two-body problem.

the reference configuration $\mathscr{B}^{(i)} \subset \mathbb{R}^3$. Furthermore, the boundary $\Gamma^{(i)}$ can be subdivided into the Neumann boundary $\Gamma_\sigma^{(i)}$, the Dirichlet boundary $\Gamma_u^{(i)}$ and the previously mentioned interface Γ_d. The current position of the boundaries $\Gamma^{(i)}$ is denoted with $\gamma^{(i)} = \boldsymbol{\varphi}^{(i)}(\Gamma^{(i)})$.

The principle of virtual work for the present domain decomposition problem can be written as

$$\sum_{i=1}^{2} (G^{(i),\mathrm{dyn}} + G^{(i),\mathrm{int}} + G^{(i),\mathrm{ext}} + G^{(i),\mathrm{d}}) = 0 \tag{1}$$

which conforms with Hamilton's principle of stationary action in the Lagrangian mechanics. The first term in (1) specifies the contribution of the inertia terms

$$G^{(i),\mathrm{dyn}}(\boldsymbol{\varphi}^{(i)}, \delta\boldsymbol{\varphi}^{(i)}) = \int_{\mathscr{B}^{(i)}} \delta\boldsymbol{\varphi}^{(i)} \cdot \rho_R \ddot{\boldsymbol{\varphi}}^{(i)} \, \mathrm{d}V \tag{2}$$

where a superposed dot denotes differentiation with respect to time, ρ_R the reference mass density and $\delta\boldsymbol{\varphi}^{(i)}$ the variation of $\boldsymbol{\varphi}^{(i)}$. The virtual work arising from the internal forces reads

$$G^{(i),\mathrm{int}}(\boldsymbol{\varphi}^{(i)}, \delta\boldsymbol{\varphi}^{(i)}) = \int_{\mathscr{B}^{(i)}} \nabla(\delta\boldsymbol{\varphi}^{(i)}) : \boldsymbol{P}^{(i)} \, \mathrm{d}V \tag{3}$$

where $\boldsymbol{P}^{(i)}$ denotes the first Piola–Kirchhoff stress tensor. The virtual work of the external forces can be decomposed into the body forces and the forces acting on the Neumann boundary

$$G^{(i),\mathrm{ext}}(\boldsymbol{\varphi}^{(i)}, \delta\boldsymbol{\varphi}^{(i)}) = \int_{\mathscr{B}^{(i)}} \rho_R \boldsymbol{B}^{(i)} \cdot \delta\boldsymbol{\varphi}^{(i)} \, \mathrm{d}V + \int_{\Gamma_\sigma} \bar{\boldsymbol{T}}^{(i)} \cdot \delta\boldsymbol{\varphi}^{(i)} \, \mathrm{d}\Gamma \tag{4}$$

where $\boldsymbol{B}^{(i)}$ denotes the applied body forces and $\bar{\boldsymbol{T}}^{(i)}$ the prescribed tractions. The virtual work of the coupling tractions for a two-parts problem is given by

$$G^{\mathrm{d}} = \sum_{i=1}^{2} G^{(i),\mathrm{d}}(\boldsymbol{\varphi}^{(i)}, \delta\boldsymbol{\varphi}^{(i)}) \tag{5}$$

with

$$G^{(i),\mathrm{d}}(\boldsymbol{\varphi}^{(i)}, \delta\boldsymbol{\varphi}^{(i)}) = \int_{\Gamma_{\mathrm{d}}^{(i)}} \boldsymbol{t}^{(i)} \cdot \delta\boldsymbol{\varphi} \, \mathrm{d}\Gamma \tag{6}$$

DOI: 10.1002/nme

where the (Piola) tractions $\boldsymbol{t}^{(i)}=[t_1,\ldots,t_{n_{\mathrm{dim}}}]$ of an n_{dim} dimensional problem are incorporated. Considering the balance of linear momentum across the interface, (5) can be expressed as follows:

$$G^{\mathrm{d}}=\int_{\Gamma_{\mathrm{d}}^{(1)}}\boldsymbol{t}^{(1)}\cdot(\delta\boldsymbol{\varphi}^{(1)}-\delta\boldsymbol{\varphi}^{(2)})\,\mathrm{d}\Gamma \tag{7}$$

Here, the integration refers to the surface (1), subsequently called the non-mortar side, whereas surface (2) will be called the mortar side.

3. FINITE ELEMENT DISCRETIZATION

Lets start by considering isoparametric displacement-based finite elements in space (see Hughes [34]) that rest on the approximations

$$\boldsymbol{\varphi}^{(i),\mathrm{h}}=\sum_{A\in\omega^{(i)}}N^A(\boldsymbol{X}^{(i)})\boldsymbol{q}_A^{(i)},\quad \delta\boldsymbol{\varphi}^{(i),\mathrm{h}}=\sum_{A\in\omega^{(i)}}N^A(\boldsymbol{X}^{(i)})\delta\boldsymbol{q}_A^{(i)} \tag{8}$$

for the discrete configuration as well as for the tractions

$$\boldsymbol{t}^{(1),\mathrm{h}}=\sum_{A\in\bar{\omega}^{(1)}}N^A(\boldsymbol{X}^{(1)})\boldsymbol{\lambda}_A \tag{9}$$

using global shape functions $N^A(\boldsymbol{X}^{(i)}):\mathscr{B}\to\mathbb{R}$ associated with nodes $A\in\omega^{(i)}=\{1,\ldots,n_{\mathrm{node}}^{(i)}\}$, where $n_{\mathrm{nodes}}^{(i)}$ denotes the total number of nodes of body (i). Furthermore, $\bar{\omega}^{(i)}=\{1,\ldots,n_{\mathrm{surf}}^{(i)}\}$, $\bar{\omega}^{(i)}\subset\omega^{(i)}$ denotes the set of nodes on the respective internal interfaces and $\boldsymbol{\lambda}_A$ the associated nodal values of the tractions. The configuration of each part (i) of the semi-discrete flexible body is characterized by its configuration vector

$$\boldsymbol{q}^{(i)}(t)=\begin{bmatrix}\boldsymbol{q}_1^{(i)}(t)\\ \vdots\\ \boldsymbol{q}_{n_{\mathrm{node}}^{(i)}}^{(i)}(t)\end{bmatrix} \tag{10}$$

For a two-parts problem the configuration of the complete semi-discrete system is given by

$$\boldsymbol{q}(t)=\begin{bmatrix}\boldsymbol{q}^{(1)}(t)\\ \boldsymbol{q}^{(2)}(t)\end{bmatrix} \tag{11}$$

Similarly, a vector of the nodal values of the tractions can be introduced with

$$\boldsymbol{\lambda}(t)=\begin{bmatrix}\boldsymbol{\lambda}_1(t)\\ \vdots\\ \boldsymbol{\lambda}_{n_{\mathrm{surf}}^{(1)}}(t)\end{bmatrix} \tag{12}$$

where each $\boldsymbol{\lambda}_A$ is uniquely defined on a single node $A\in\bar{\omega}^{(1)}$ of the internal surface of part $i=1$, assuming that the Lagrange multipliers are defined on this specific surface. Now, the discrete

DOI: 10.1002/nme

counterpart of (1) can be constructed systematically by making use of the afore established discrete quantities. The discrete counterpart of the inertia terms can be written as

$$G^{\mathrm{dyn}}(\boldsymbol{\varphi}^{\mathrm{h}}, \delta\boldsymbol{\varphi}^{\mathrm{h}}) = \delta\boldsymbol{q} \cdot \boldsymbol{M}\ddot{\boldsymbol{q}} \tag{13}$$

where the coefficients of the discrete mass matrix

$$\boldsymbol{M}^{AB} = \int_{\mathscr{B}} \rho_R N^A N^B \,\mathrm{d}V \boldsymbol{I} \tag{14}$$

are introduced together with the variations $\delta\boldsymbol{q}$ of the discrete configuration. For the virtual work of the internal forces, the discretized deformation gradient and deformation tensor have to be incorporated using

$$\boldsymbol{F}^{(i),\mathrm{h}} = \frac{\delta\boldsymbol{\varphi}^{(i),\mathrm{h}}}{\delta\boldsymbol{X}^{(i)}} = \sum_{A \in \omega^{(i)}} \boldsymbol{q}_A^{(i)} \otimes \nabla N^A(\boldsymbol{X}^{(i)}) \tag{15}$$

and

$$\boldsymbol{C}^{(i),\mathrm{h}} = \sum_{A,B \in \omega^{(i)}} \boldsymbol{q}_A^{(i)} \cdot \boldsymbol{q}_B^{(i)} \nabla N^A(\boldsymbol{X}^{(i)}) \otimes \nabla N^B(\boldsymbol{X}^{(i)}) \tag{16}$$

The semi-discrete formulation of the two-body system at hand can be associated with a potential energy function of the form

$$V(\boldsymbol{q}) = \sum_{i=1}^{2} (V^{(i),\mathrm{int}}(\boldsymbol{q}^{(i)}) + V^{(i),\mathrm{ext}}(\boldsymbol{q}^{(i)})) \tag{17}$$

which is decomposed into a strain energy function

$$V^{(i),\mathrm{int}}(\boldsymbol{q}^{(i)}) = \int_{\mathscr{B}^{(i)}} W(\boldsymbol{C}^{(i),\mathrm{h}}) \,\mathrm{d}V \tag{18}$$

using an energy density function $W(\boldsymbol{C}^{(i),\mathrm{h}})$ and the external potential energy function

$$V^{(i),\mathrm{ext}}(\boldsymbol{q}^{(i)}) = \sum_{A \in \omega^{(i)}} \boldsymbol{q}_A^{(i)} \cdot \left(\int_{\mathscr{B}^{(i)}} N^A \boldsymbol{B}^{(i)} \,\mathrm{d}V + \int_{\Gamma_\sigma^{(i)}} N^A \bar{\boldsymbol{T}}^{(i)} \,\mathrm{d}\Gamma \right) \tag{19}$$

The discrete virtual work expression corresponding to (3) can be written as

$$G^{(i),\mathrm{int}}(\boldsymbol{\varphi}^{(i),\mathrm{h}}, \delta\boldsymbol{\varphi}^{(i),\mathrm{h}}) = \sum_{A,B \in \omega^{(i)}} \delta\boldsymbol{q}_A^{(i)} \cdot \boldsymbol{q}_B^{(i)} \int_{\mathscr{B}^{(i)}} \nabla N^A(\boldsymbol{X}^{(i)}) \cdot \boldsymbol{S}(\boldsymbol{C}^{(i),\mathrm{h}}) \nabla N^B(\boldsymbol{X}^{(i)}) \,\mathrm{d}V \tag{20}$$

where $\boldsymbol{S}(\boldsymbol{C}^{(i),\mathrm{h}}) = 2\partial W / \partial \boldsymbol{C}^{(i),\mathrm{h}}$ denotes the second Piola–Kirchhoff stress tensor. The discrete virtual work expression corresponding to (19) can be derived as

$$G^{(i),\mathrm{ext}}(\boldsymbol{\varphi}^{(i),\mathrm{h}}, \delta\boldsymbol{\varphi}^{(i),\mathrm{h}}) = \nabla V^{(i),\mathrm{ext}}(\boldsymbol{q}^{(i)}) \cdot \delta\boldsymbol{q}^{(i)} \tag{21}$$

DOI: 10.1002/nme

3.1. Discrete mesh-tying constraints

We now turn to the formulation of appropriate mortar-based mesh-tying constraints. For finite-deformation problems, these constraints are required to conform with fundamental conservation laws of mechanics such as conservation of linear and angular momentums, respectively.

Inserting the approximations (8) and (9) into (7) yields the contribution of the discrete interface forces to the virtual work:

$$\begin{aligned} G^{\mathrm{d}}(\boldsymbol{\varphi}^{\mathrm{h}}, \boldsymbol{t}^{(1),\mathrm{h}}; \delta\boldsymbol{\varphi}^{\mathrm{h}}) &= \int_{\Gamma_{\mathrm{d}}^{(1)}} \boldsymbol{t}^{(1),\mathrm{h}} \cdot (\delta\boldsymbol{\varphi}^{(1),\mathrm{h}} - \delta\boldsymbol{\varphi}^{(2),\mathrm{h}})\, \mathrm{d}\Gamma \\ &= \sum_A \boldsymbol{\lambda}_A \cdot \left(\sum_B n^{AB} \delta\boldsymbol{q}_B^{(1)} - \sum_C n^{AC} \delta\boldsymbol{q}_C^{(2)} \right) \end{aligned} \tag{22}$$

where n^{AB} and n^{AC} denote the so-called mortar integrals given by

$$\begin{aligned} n^{AB} &= \int_{\Gamma_{\mathrm{d}}^{(1)}} N^A(\boldsymbol{X}^{(1)}) N^B(\boldsymbol{X}^{(1)})\, \mathrm{d}\Gamma \\ n^{AC} &= \int_{\Gamma_{\mathrm{d}}^{(1)}} N^A(\boldsymbol{X}^{(1)}) N^C(\boldsymbol{X}^{(2)})\, \mathrm{d}\Gamma \end{aligned} \tag{23}$$

To facilitate (a) conservation of linear momentum and (b) conservation of angular momentum in the discrete setting, the following conditions have to be satisfied:

(a) $G^{\mathrm{d}}(\boldsymbol{\varphi}^{\mathrm{h}}, \boldsymbol{t}^{(1),\mathrm{h}}; \boldsymbol{\mu}) = 0$
(b) $G^{\mathrm{d}}(\boldsymbol{\varphi}^{\mathrm{h}}, \boldsymbol{t}^{(1),\mathrm{h}}; \boldsymbol{\mu} \times \boldsymbol{\varphi}^{\mathrm{h}}) = 0$

for any $\boldsymbol{\mu} \in \mathbb{R}^3$. The fulfillment of these conditions places certain restrictions on the specific form of the mesh-tying constraints, which eventually determine the Lagrange multipliers $\boldsymbol{\lambda}_A$. Inserting the nodal pattern $\delta\boldsymbol{q}_I^{(i)} = \boldsymbol{\mu}$ into (22) yields

$$\boldsymbol{\mu} \cdot \left\{ \sum_A \boldsymbol{\lambda}_A \int_{\Gamma_{\mathrm{d}}^{(1)}} N^A(\boldsymbol{X}^{(1)}) \left(\left[\sum_B N^B(\boldsymbol{X}^{(1)}) \right] - \left[\sum_C N^C(\boldsymbol{X}^{(2)}) \right] \right) \mathrm{d}\Gamma \right\} \tag{24}$$

Accordingly, due to the completeness property of the shape functions, i.e. $\sum_I N^I(\boldsymbol{X}^{(i)}) = 1$, condition (a) is satisfied, thus facilitating conservation of linear momentum.

Inserting the nodal pattern $\delta\boldsymbol{q}_I^{(i)} = \boldsymbol{\mu} \times \boldsymbol{q}^{(i)}$ into (22) yields

$$-\boldsymbol{\mu} \cdot \left\{ \sum_A \boldsymbol{\lambda}_A \times \left(\sum_B n^{AB} \boldsymbol{q}_B^{(1)} - \sum_C n^{AC} \boldsymbol{q}_C^{(2)} \right) \right\} \tag{25}$$

Accordingly, to satisfy condition (b) the discrete mesh-tying constraints

$$\boldsymbol{\Phi}^A = \sum_B n^{AB} \boldsymbol{q}_B^{(1)} - \sum_C n^{AC} \boldsymbol{q}_C^{(2)} = \boldsymbol{0} \tag{26}$$

need to be satisfied. Introducing the nodal displacements $\boldsymbol{u}_I^{(i)} \in \mathbb{R}^3$, such that

$$\boldsymbol{q}_I^{(i)} = \boldsymbol{X}_I^{(i)} + \boldsymbol{u}_I^{(i)} \tag{27}$$

DOI: 10.1002/nme

the constraints in (26) can be recast as

$$\boldsymbol{\Phi}^A = \underbrace{\sum_B n^{AB}\boldsymbol{u}_B^{(1)} - \sum_C n^{AC}\boldsymbol{u}_C^{(2)}}_{\boldsymbol{\Phi}_u^A} + \underbrace{\sum_B n^{AB}\boldsymbol{X}_B^{(1)} - \sum_C n^{AC}\boldsymbol{X}_C^{(2)}}_{\boldsymbol{\Phi}_X^A} = \boldsymbol{0} \tag{28}$$

Here, the first part, $\boldsymbol{\Phi}_u^A$, can be identified as the displacement form of the mortar constraints (see Puso [16]). Consequently, if $\boldsymbol{\Phi}_u^A = \boldsymbol{0}$ is enforced, conservation of angular momentum demands that $\boldsymbol{\Phi}_X^A = \boldsymbol{0}$. That is, the mortar constraints need to be satisfied in the reference configuration too. In general, this requirement necessitates a mesh initialization procedure for repositioning the non-mortar nodes in the reference configuration (see Puso [16] for further details). Alternatively, if node relocation is undesirable, Puso outlines the use of vectors attached to element frames to rotate the constraints.

Strictly speaking, changing the initial position of interface nodes contradicts the original idea of tying independently generated meshes. Therefore, we aim at a reformulation of the mortar constraints that does not necessitate any changes of the initial mesh but still preserves the fundamental conservation laws. For simplicity of exposition, we first deal with the node to surface method that can be viewed as degenerated version of the mortar method. We then proceed with the advocated reformulation of the mortar constraints.

4. NODE-TO-SURFACE METHOD

To illustrate our approach to the design of frame-indifferent mesh-tying constraints, we first deal with the NTS method. To this end we consider a representative NTS element depicted in Figure 2. The NTS constraints can be obtained from the mortar constraints (26) by setting

$$\begin{aligned} N^A(\boldsymbol{X}^{(1)}) &\to N^A(\boldsymbol{X}_S^{(1)}) = \delta^{AS} \\ \boldsymbol{t}^{(1),\mathrm{h}} &\to \boldsymbol{\lambda}_S \\ \boldsymbol{\varphi}^{(1),\mathrm{h}} &\to \boldsymbol{q}_S^{(1)} \\ \boldsymbol{\varphi}^{(2),\mathrm{h}} &\to \hat{\boldsymbol{\varphi}}^{(2)}(\boldsymbol{\xi}) = \sum_{C=1}^{4} \hat{N}^C(\boldsymbol{\xi})\boldsymbol{q}_c^{(2)} \end{aligned} \tag{29}$$

Here, $\boldsymbol{X}_S^{(1)}$ denotes a material point on $\Gamma^{(1),\mathrm{h}}$, which coincides with the slave node S. Correspondingly, $\boldsymbol{q}_S^{(1)} \in \mathbb{R}^3$ is the position vector of the slave node in the current configuration. The tractions $\boldsymbol{t}^{(1),\mathrm{h}}$ degenerate to the nodal force vector $\boldsymbol{\lambda}_S \in \mathbb{R}^3$. Moreover $\hat{\boldsymbol{\varphi}}^{(2)}(\boldsymbol{\xi})$ represents the surface $\Gamma^{(2),\mathrm{h}}$, parameterized in terms of local convected coordinates $\boldsymbol{\xi} = (\xi_1, \xi_2)$. In the present work we restrict our attention to isoparametric tri-linear solid elements, so that $\hat{N}^C(\boldsymbol{\xi})$ are standard bi-linear local shape functions. Consequently, the placement of material points belonging to the discrete interface surface $\Gamma^{(2),\mathrm{h}}$ in the reference configuration follows from

$$\boldsymbol{X}^{(2),h}(\boldsymbol{\xi}) = \sum_{C=1}^{4} \hat{N}^C(\boldsymbol{\xi})\boldsymbol{X}_C^{(2)} \tag{30}$$

DOI: 10.1002/nme

To simplify notation it will prove convenient to introduce the ordered set η^S of vectors relevant to the representative NTS element under consideration:

$$\eta^S = \{\boldsymbol{y}_1, \dots, \boldsymbol{y}_5\} = \{\boldsymbol{q}_S^{(1)}, \boldsymbol{q}_1^{(2)}, \boldsymbol{q}_2^{(2)}, \boldsymbol{q}_3^{(2)}, \boldsymbol{q}_4^{(2)}\} \tag{31}$$

Taking into account (29), the mortar integrals degenerate to

$$\begin{aligned} n^{AB} &= \delta^{AS}\delta^{BS} \\ n^{AC} &= \delta^{AS}\hat{N}^C(\bar{\boldsymbol{\xi}}) \end{aligned} \tag{32}$$

Accordingly, the constraints (26) boil down to the collocation form

$$\boldsymbol{\Phi}^S(\boldsymbol{y}_I) = \boldsymbol{q}_S^{(1)} - \sum_{C=1}^{4} \hat{N}^C(\bar{\boldsymbol{\xi}})\boldsymbol{q}_C^{(2)} = \boldsymbol{0} \tag{33}$$

In this connection, $\bar{\boldsymbol{\xi}}$ characterizes the position of a point on the surface $\Gamma^{(2),\mathrm{h}}$ resulting from a closest point projection of the slave node. For the domain decomposition problem under consideration, $\bar{\boldsymbol{\xi}}$ is assumed to be constant and can be calculated once at problem initialization. To determine $\bar{\boldsymbol{\xi}}$, the following system of non-linear equations:

$$\left[\boldsymbol{X}_S^{(1)} - \sum_{C=1}^{4} \hat{N}^C(\bar{\boldsymbol{\xi}})\boldsymbol{X}_C^{(2)}\right] \cdot \boldsymbol{A}_\alpha(\bar{\boldsymbol{\xi}}) = 0 \quad (\alpha = 1, 2) \tag{34}$$

needs to be solved iteratively (see, for example, Wriggers [9]). In the last equation

$$\boldsymbol{A}_\alpha(\boldsymbol{\xi}) = \sum_{B=1}^{4} \hat{N}^B_{,\alpha}(\boldsymbol{\xi})\boldsymbol{X}_B^{(2)} \tag{35}$$

denote convective base vectors in the initial configuration. In particular, $\boldsymbol{A}_1(\boldsymbol{\xi})$ and $\boldsymbol{A}_2(\boldsymbol{\xi})$ span the tangent plane of the surface $\Gamma^{(2),\mathrm{h}}$ at $\boldsymbol{X}^{(2),h}(\boldsymbol{\xi})$. Note that, similar to the decomposition (28), the NTS constraint (33) can be recast in the form

$$\boldsymbol{\Phi}^S = \underbrace{\boldsymbol{u}_S^{(1)} - \sum_C \hat{N}^C(\bar{\boldsymbol{\xi}})\boldsymbol{u}_C^{(2)}}_{\boldsymbol{\Phi}_u^S} + \underbrace{\boldsymbol{X}_S^{(1)} - \sum_C \hat{N}^C(\bar{\boldsymbol{\xi}})\boldsymbol{X}_C^{(2)}}_{\boldsymbol{\Phi}_X^S} = \boldsymbol{0} \tag{36}$$

Accordingly, in the context of the NTS method, application of the repositioning procedure results in moving the slave node $\boldsymbol{X}_S^{(1)}$ to the surface $\Gamma^{(2),\mathrm{h}}$ at $\boldsymbol{X}^{(2),h}(\bar{\boldsymbol{\xi}})$ such that $\boldsymbol{\Phi}_X^S = \boldsymbol{0}$. To circumvent the need for changing the initial position of the slave node, we next propose a specific reformulation of the NTS constraints (33).

4.1. Reformulation of the NTS constraints

In this section we propose an alternative formulation of the NTS constraints (33) that makes possible to retain conservation of both linear and angular momentums without resorting to the nodal repositioning procedure. In general domain decomposition problems, the slave nodes do

DOI: 10.1002/nme

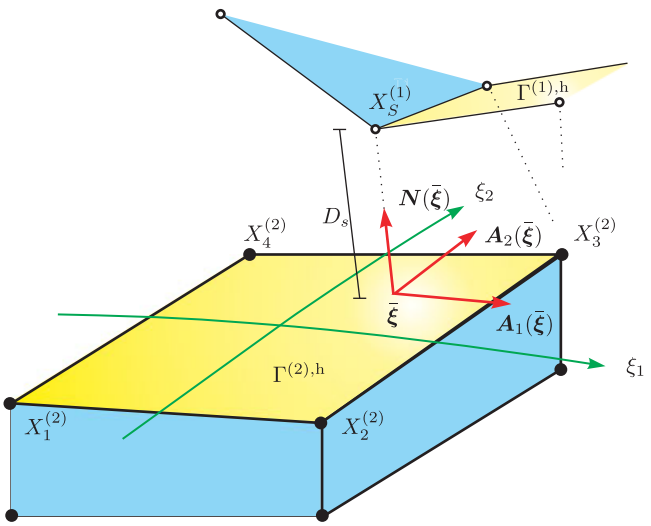

Figure 2. Initial configuration of the representative NTS element: closest point projection of the slave node $X_S^{(1)}$ onto the surface $\Gamma^{(2),\mathrm{h}}$.

not lie on the surface $\Gamma^{(2),\mathrm{h}}$. That is, $\mathbf{\Phi}_X^S \neq \mathbf{0}$ in general. The closest point projection for the determination of $\bar{\boldsymbol{\xi}}$ in (34) implies that

$$\left[\boldsymbol{X}_S^{(1)} - \sum_{C=1}^{4} \hat{N}^C(\bar{\boldsymbol{\xi}})\boldsymbol{X}_C^{(2)}\right] \cdot \boldsymbol{N}(\bar{\boldsymbol{\xi}}) = D_S \tag{37}$$

where $\boldsymbol{N}(\bar{\boldsymbol{\xi}})$ is the normal to the tangent plane spanned by $\boldsymbol{A}_1(\bar{\boldsymbol{\xi}})$ and $\boldsymbol{A}_2(\bar{\boldsymbol{\xi}})$ given by

$$\boldsymbol{N}(\bar{\boldsymbol{\xi}}) = \frac{\boldsymbol{A}_1(\bar{\boldsymbol{\xi}}) \times \boldsymbol{A}_2(\bar{\boldsymbol{\xi}})}{\|\boldsymbol{A}_1(\bar{\boldsymbol{\xi}}) \times \boldsymbol{A}_2(\bar{\boldsymbol{\xi}})\|} \tag{38}$$

and D_S denotes the minimal distance of the slave node $\boldsymbol{X}_S^{(1)}$ to the tangent plane at $\boldsymbol{X}^{(2),h}(\bar{\boldsymbol{\xi}})$ in the initial configuration (see Figure 2). Bearing in mind that both $\bar{\boldsymbol{\xi}}$ and D_S are computed once at problem initialization, we now define the modified NTS constraints as

$$\begin{aligned} \bar{\Phi}_\alpha^S(\boldsymbol{y}_I) &= \mathbf{\Phi}^S(\boldsymbol{y}_I) \cdot \boldsymbol{a}_\alpha(\bar{\boldsymbol{\xi}}) = 0 \quad (\alpha = 1, 2) \\ \bar{\Phi}_3^S(\boldsymbol{y}_I) &= \mathbf{\Phi}^S(\boldsymbol{y}_I) \cdot \boldsymbol{n}(\bar{\boldsymbol{\xi}}) - D_S = 0 \end{aligned} \tag{39}$$

where

$$\boldsymbol{a}_\alpha(\bar{\boldsymbol{\xi}}) = \sum_{B=1}^{4} \hat{N}_{,\alpha}^B(\bar{\boldsymbol{\xi}})\boldsymbol{q}_B^{(2)} \tag{40}$$

and

$$\boldsymbol{n}(\bar{\boldsymbol{\xi}}) = \frac{\boldsymbol{a}_1(\bar{\boldsymbol{\xi}}) \times \boldsymbol{a}_2(\bar{\boldsymbol{\xi}})}{\|\boldsymbol{a}_1(\bar{\boldsymbol{\xi}}) \times \boldsymbol{a}_2(\bar{\boldsymbol{\xi}})\|} \tag{41}$$

DOI: 10.1002/nme

The modified NTS constraints (39) enforce the fixed distance D_S between the current placement of the slave node S and the point $\hat{\boldsymbol{\varphi}}^{(2)}(\bar{\boldsymbol{\xi}})$ on the current surface $\gamma^{(2),\mathrm{h}}$ through the orthogonal projection of S onto the plane spanned by the convective base vectors $\boldsymbol{a}_1(\bar{\boldsymbol{\xi}})$ and $\boldsymbol{a}_2(\bar{\boldsymbol{\xi}})$. Note that the modified NTS constraints (39) coincide with the original ones in (33) if $D_S=0$.

4.2. Frame-indifference of the modified NTS constraints

It can be easily verified that the modified NTS constraints (39) are frame-indifferent (or objective). To see this, consider rigid motions of the form

$$\boldsymbol{y}_I^\sharp = \boldsymbol{c} + \boldsymbol{Q}\boldsymbol{y}_I \tag{42}$$

where $\boldsymbol{c}\in\mathbb{R}^3$, and $\boldsymbol{Q}\in SO(3)$ is a rotation tensor. With regard to the convective base vectors (40) one gets

$$\boldsymbol{a}_\alpha^\sharp = \sum_{B=1}^{4} \hat{N}^B_{,\alpha}[\boldsymbol{c}+\boldsymbol{Q}\boldsymbol{q}_B^{(2)}] = \boldsymbol{Q}\sum_{B=1}^{4} \hat{N}^B_{,\alpha}\boldsymbol{q}_B^{(2)} = \boldsymbol{Q}\boldsymbol{a}_\alpha \tag{43}$$

where again use has been made of the completeness property of the nodal shape functions. Moreover,

$$\boldsymbol{n}^\sharp = \frac{\boldsymbol{a}_1^\sharp\times\boldsymbol{a}_2^\sharp}{\|\boldsymbol{a}_1^\sharp\times\boldsymbol{a}_2^\sharp\|} = \frac{\boldsymbol{Q}\boldsymbol{a}_1\times\boldsymbol{Q}\boldsymbol{a}_2}{\|\boldsymbol{Q}\boldsymbol{a}_1\times\boldsymbol{Q}\boldsymbol{a}_2\|} = \frac{\boldsymbol{Q}(\boldsymbol{a}_1\times\boldsymbol{a}_2)}{\|\boldsymbol{Q}(\boldsymbol{a}_1\times\boldsymbol{a}_2)\|} = \boldsymbol{Q}\boldsymbol{n} \tag{44}$$

Concerning the original NTS constraints (33) one gets

$$\begin{aligned}
\boldsymbol{\Phi}^S(\boldsymbol{y}_I^\sharp) &= \boldsymbol{q}_S^{(1)^\sharp} - \sum_{C=1}^{4} \hat{N}^C(\bar{\boldsymbol{\xi}})\boldsymbol{q}_C^{(2)^\sharp} \\
&= \boldsymbol{c} + \boldsymbol{Q}\boldsymbol{q}_S^{(1)} - \sum_{C=1}^{4} \hat{N}^C(\bar{\boldsymbol{\xi}})[\boldsymbol{c}+\boldsymbol{Q}\boldsymbol{q}_C^{(2)}] \\
&= \boldsymbol{Q}\left[\boldsymbol{q}_S^{(1)} - \sum_{C=1}^{4} \hat{N}^C(\bar{\boldsymbol{\xi}})\boldsymbol{q}_C^{(2)}\right] \\
&= \boldsymbol{Q}\boldsymbol{\Phi}^S(\boldsymbol{y}_I)
\end{aligned} \tag{45}$$

Now the frame-indifference of the modified NTS constraints $\bar{\Phi}_i^S(\boldsymbol{y}_I)$ in (39) can be confirmed. Specifically,

$$\bar{\Phi}_\alpha^S(\boldsymbol{y}_I^\sharp) = \boldsymbol{\Phi}^S(\boldsymbol{y}_I^\sharp)\cdot\boldsymbol{a}_\alpha^\sharp(\bar{\boldsymbol{\xi}}) = \boldsymbol{\Phi}^S(\boldsymbol{y}_I)\cdot\boldsymbol{Q}^{\mathrm{T}}\boldsymbol{Q}\boldsymbol{a}_\alpha(\bar{\boldsymbol{\xi}}) = \boldsymbol{\Phi}^S(\boldsymbol{y}_I)\cdot\boldsymbol{a}_\alpha(\bar{\boldsymbol{\xi}}) = \bar{\Phi}_\alpha^S(\boldsymbol{y}_I) \tag{46}$$

for $\alpha=1,2$. Similarly,

$$\bar{\Phi}_3^S(\boldsymbol{y}_I^\sharp) = \bar{\Phi}_3^S(\boldsymbol{y}_I) \tag{47}$$

DOI: 10.1002/nme

The contribution of the representative NTS element to the virtual work (22) of the interface forces can be written as

$$G^{d,S} = \boldsymbol{\lambda}_S \cdot \left(\sum_{I=1}^{5} (\partial_{\boldsymbol{y}_I} \bar{\boldsymbol{\Phi}}^S) \delta \boldsymbol{y}_I \right) \tag{48}$$

where $\bar{\boldsymbol{\Phi}}^S = [\bar{\Phi}_1^S, \bar{\Phi}_2^S, \bar{\Phi}_3^S]^{\mathrm{T}}$. Frame-indifference of the modified NTS constraints implies the translational invariance property $\bar{\boldsymbol{\Phi}}^S(\boldsymbol{y}_I + \varepsilon \boldsymbol{\mu}) = \bar{\boldsymbol{\Phi}}^S(\boldsymbol{y}_I)$ for arbitrary $\varepsilon \in \mathbb{R}$. Consequently,

$$\boldsymbol{0} = \frac{\mathrm{d}}{\mathrm{d}\varepsilon}\bigg|_{\varepsilon=0} \bar{\boldsymbol{\Phi}}^S(\boldsymbol{y}_I + \varepsilon \boldsymbol{\mu}) = \sum_{I=1}^{5} (\partial_{\boldsymbol{y}_I} \bar{\boldsymbol{\Phi}}^S) \boldsymbol{\mu} \tag{49}$$

In the context of the NTS method, the last equation implies the fulfillment of condition (a) for conservation of linear momentum. Similarly, frame-indifference of the modified NTS constraints implies the rotational invariance property $\bar{\boldsymbol{\Phi}}^S(\exp(\varepsilon \widehat{\boldsymbol{\mu}}) \boldsymbol{y}_I) = \bar{\boldsymbol{\Phi}}^S(\boldsymbol{y}_I)$ for arbitrary $\varepsilon \in \mathbb{R}$. Here, $\exp(\widehat{\boldsymbol{\mu}}) \in SO(3)$ denotes the exponential map of a skew-symmetric tensor $\widehat{\boldsymbol{\mu}}$, which can be associated with an axial vector $\boldsymbol{\mu} \in \mathbb{R}^3$, such that $\widehat{\boldsymbol{\mu}} \boldsymbol{a} = \boldsymbol{\mu} \times \boldsymbol{a}$ for any $\boldsymbol{a} \in \mathbb{R}^3$. Owing to rotational invariance, one gets

$$\boldsymbol{0} = \frac{\mathrm{d}}{\mathrm{d}\varepsilon}\bigg|_{\varepsilon=0} \bar{\boldsymbol{\Phi}}^S(\exp(\varepsilon \widehat{\boldsymbol{\mu}}) \boldsymbol{y}_I) = \sum_{I=1}^{5} (\partial_{\boldsymbol{y}_I} \bar{\boldsymbol{\Phi}}^S)(\boldsymbol{\mu} \times \boldsymbol{y}_I) \tag{50}$$

The last equation implies satisfaction of condition (b) for conservation of angular momentum in the context of the NTS method.

The rotational invariance property of the modified NTS constraints is in agreement with Cauchy's representation theorem (see Truesdell and Noll [35, Section 11] or Antman [36, Chapter 8]). In particular, rotational invariance of $\bar{\Phi}_\alpha^S(\boldsymbol{y}_I)$ in $(39)_1$ follows from the fact these constraints depend only on the set of invariants

$$\mathbb{S}(\eta^S) = \{\boldsymbol{y}_I \cdot \boldsymbol{y}_J,\ 1 \leqslant I \leqslant J \leqslant 5\} \tag{51}$$

Moreover, the constraint $\bar{\Phi}_3^S(\boldsymbol{y}_I)$ in $(39)_2$ is invariant under rotations, for it depends only on the set of invariants $\mathbb{S}(\eta^S) \cup \mathbb{T}(\eta^S)$, where

$$\mathbb{T}(\eta^S) = \{(\boldsymbol{y}_I \times \boldsymbol{y}_J) \cdot \boldsymbol{y}_K,\ 1 \leqslant I < J < K \leqslant 5\} \tag{52}$$

Note that the invariants in $\mathbb{T}(\eta^S)$ are cubic functions of the nodal coordinates, whereas $\mathbb{S}(\eta^S)$ contains only quadratic invariants. The presence of cubic invariants distinguishes the three-dimensional case from the two-dimensional case where merely quadratic invariants are present (see Hesch and Betsch [33]). Since our conserving time discretization requires invariants that are at most quadratic, we aim at a reformulation of the constraint $(39)_2$ that avoids the use of cubic invariants.

4.3. Augmented coordinates

We next aim at a reformulation of the modified NTS constraint $(39)_2$ in terms of invariants being at most quadratic. To this end, we apply a specific coordinate augmentation technique originally

DOI: 10.1002/nme

introduced by Betsch and Uhlar [37] in the context of multibody dynamics for the description of joint-coordinates and conjugate joint-forces.

In the context of the representative NTS element we introduce additional coordinates $\boldsymbol{d}_S \in \mathbb{R}^3$, which are appended to the original set η^S of relevant vectors in (31). Accordingly, the coordinate augmentation yields the extended set of vectors

$$\eta^{S,\mathrm{aug}} = \{\boldsymbol{y}_1, \ldots, \boldsymbol{y}_5, \boldsymbol{d}_S\} \tag{53}$$

To link the new coordinates to the original ones, the following three additional constraint functions are defined:

$$\boldsymbol{\Phi}^{\mathrm{aug}}(\boldsymbol{y}_I, \boldsymbol{d}_S) = \begin{bmatrix} \boldsymbol{d}_S \cdot \boldsymbol{a}_1(\bar{\xi}) \\ \boldsymbol{d}_S \cdot \boldsymbol{a}_2(\bar{\xi}) \\ \frac{1}{2}(\boldsymbol{d}_S \cdot \boldsymbol{d}_S - 1) \end{bmatrix} \tag{54}$$

If these additional constraints are satisfied, i.e. $\boldsymbol{\Phi}^{\mathrm{aug}} = \boldsymbol{0}$, then the newly introduced vector $\boldsymbol{d}_S$ plays the role of the unit normal vector (41). This can be easily verified by substituting $\boldsymbol{n}(\bar{\xi})$ from (41) for $\boldsymbol{d}_S$ in (54). For later use we note that the following property holds:

$$\begin{aligned} \boldsymbol{\Phi}^{\mathrm{aug}}(\boldsymbol{c} + \boldsymbol{Q}\boldsymbol{y}_I, \boldsymbol{d}_S) &= \begin{bmatrix} \boldsymbol{d}_S \cdot \boldsymbol{Q}\boldsymbol{a}_1(\bar{\xi}) \\ \boldsymbol{d}_S \cdot \boldsymbol{Q}\boldsymbol{a}_2(\bar{\xi}) \\ \frac{1}{2}(\boldsymbol{d}_S \cdot \boldsymbol{d}_S - 1) \end{bmatrix} \\ &= \begin{bmatrix} \boldsymbol{a}_1(\bar{\xi}) \cdot \boldsymbol{Q}^{\mathrm{T}}\boldsymbol{d}_S \\ \boldsymbol{a}_2(\bar{\xi}) \cdot \boldsymbol{Q}^{\mathrm{T}}\boldsymbol{d}_S \\ \frac{1}{2}((\boldsymbol{Q}^{\mathrm{T}}\boldsymbol{d}_S) \cdot (\boldsymbol{Q}^{\mathrm{T}}\boldsymbol{d}_S) - 1) \end{bmatrix} = \boldsymbol{\Phi}^{\mathrm{aug}}(\boldsymbol{y}_I, \boldsymbol{Q}^{\mathrm{T}}\boldsymbol{d}_S) \end{aligned} \tag{55}$$

where use has been made of (43). Substituting $\boldsymbol{c} = \boldsymbol{0}$ and $\boldsymbol{Q} = \exp(\varepsilon\widehat{\boldsymbol{\mu}})$ into the last equation yields

$$\boldsymbol{\Phi}^{\mathrm{aug}}(\exp(\varepsilon\widehat{\boldsymbol{\mu}})\boldsymbol{y}_I, \boldsymbol{d}_S) - \boldsymbol{\Phi}^{\mathrm{aug}}(\boldsymbol{y}_I, \exp(-\varepsilon\widehat{\boldsymbol{\mu}})\boldsymbol{d}_S) = \boldsymbol{0} \tag{56}$$

Accordingly, we get

$$\begin{aligned} \left.\frac{\mathrm{d}}{\mathrm{d}\varepsilon}\right|_{\varepsilon=0} [\boldsymbol{\Phi}^{\mathrm{aug}}(\exp(\varepsilon\widehat{\boldsymbol{\mu}})\boldsymbol{y}_I, \boldsymbol{d}_S) - \boldsymbol{\Phi}^{\mathrm{aug}}(\boldsymbol{y}_I, \exp(-\varepsilon\widehat{\boldsymbol{\mu}})\boldsymbol{d}_S)] &= \boldsymbol{0} \\ \sum_{I=1}^{5} (\partial_{\boldsymbol{y}_I}\boldsymbol{\Phi}^{\mathrm{aug}})\widehat{\boldsymbol{\mu}}\boldsymbol{y}_I + (\partial_{\boldsymbol{d}_S}\boldsymbol{\Phi}^{\mathrm{aug}})\widehat{\boldsymbol{\mu}}\boldsymbol{d}_S &= \boldsymbol{0} \\ \left(\sum_{I=1}^{5} (\partial_{\boldsymbol{y}_I}\boldsymbol{\Phi}^{\mathrm{aug}})\widehat{\boldsymbol{y}}_I + (\partial_{\boldsymbol{d}_S}\boldsymbol{\Phi}^{\mathrm{aug}})\widehat{\boldsymbol{d}}_S\right)\boldsymbol{\mu} &= \boldsymbol{0} \end{aligned} \tag{57}$$

for any vector $\boldsymbol{\mu} \in \mathbb{R}^3$. This result will turn out to be crucial for conservation of angular momentum.

The modified NTS constraint $(39)_2$ can be recast by employing the augmented coordinates to obtain

$$\tilde{\Phi}_3^S(\boldsymbol{y}_I, \boldsymbol{d}_S) = \boldsymbol{\Phi}^S(\boldsymbol{y}_I) \cdot \boldsymbol{d}_S - D_S = 0 \tag{58}$$

DOI: 10.1002/nme

Note that the constraint $\tilde{\Phi}_3^S$ is a quadratic function of the augmented coordinates. In particular, it depends on the set of *quadratic* expressions

$$\widetilde{\mathbb{S}}(\eta^{S,\mathrm{aug}}) = \{\boldsymbol{y}_I \cdot \boldsymbol{d}_S\,,\, I = 1,\ldots,5\} \tag{59}$$

To summarize, the modified NTS constraints can be expressed exclusively in terms of the quadratic expressions in $\mathbb{S}(\eta^S) \cup \widetilde{\mathbb{S}}(\eta^{S,\mathrm{aug}})$. In particular

$$\tilde{\boldsymbol{\Phi}}^S(\boldsymbol{y}_I, \boldsymbol{d}_S) = \begin{bmatrix} \bar{\Phi}_1^S(\boldsymbol{y}_I) \\ \bar{\Phi}_2^S(\boldsymbol{y}_I) \\ \tilde{\Phi}_3^S(\boldsymbol{y}_I, \boldsymbol{d}_S) \end{bmatrix} = \begin{bmatrix} \boldsymbol{\Phi}^S(\boldsymbol{y}_I) \cdot \boldsymbol{a}_1(\bar{\boldsymbol{\xi}}) \\ \boldsymbol{\Phi}^S(\boldsymbol{y}_I) \cdot \boldsymbol{a}_2(\bar{\boldsymbol{\xi}}) \\ \boldsymbol{\Phi}^S(\boldsymbol{y}_I) \cdot \boldsymbol{d}_S - D_S \end{bmatrix} \tag{60}$$

Similarly, the constraints (54) due to the coordinate augmentation only depend on the quadratic expressions in $\widetilde{\mathbb{S}}(\eta^{S,\mathrm{aug}}) \cup \{\boldsymbol{d}_S \cdot \boldsymbol{d}_S\}$. We further remark that, similar to (55),

$$\tilde{\boldsymbol{\Phi}}^S(\boldsymbol{c} + \boldsymbol{Q}\boldsymbol{y}_I, \boldsymbol{d}_S) = \tilde{\boldsymbol{\Phi}}^S(\boldsymbol{y}_I, \boldsymbol{Q}^{\mathrm{T}}\boldsymbol{d}_S) \tag{61}$$

which implies

$$\left(\sum_{I=1}^{5} (\partial_{\boldsymbol{y}_I} \boldsymbol{\Phi}^S) \widehat{\boldsymbol{y}}_I + (\partial_{\boldsymbol{d}_S} \boldsymbol{\Phi}^S) \widehat{\boldsymbol{d}}_S \right) \boldsymbol{\mu} = \boldsymbol{0} \tag{62}$$

for any vector $\boldsymbol{\mu} \in \mathbb{R}^3$. The last equation can be verified along the lines of (57).

To summarize, the modified NTS mesh-tying constraints (60) and the constraints (54) due to the coordinate augmentation can be arranged in the vector of constraint functions

$$\boldsymbol{g}^S(\boldsymbol{y}_I, \boldsymbol{d}_S) = \begin{bmatrix} \tilde{\boldsymbol{\Phi}}^S(\boldsymbol{y}_I, \boldsymbol{d}_S) \\ \boldsymbol{\Phi}^{\mathrm{aug}}(\boldsymbol{y}_I, \boldsymbol{d}_S) \end{bmatrix} \tag{63}$$

pertaining to the representative NTS element. Moreover, in view of the properties (55), (61), and $(57)_3$, (62), we get

$$\begin{aligned} &\boldsymbol{g}^S(\boldsymbol{c} + \boldsymbol{Q}\boldsymbol{y}_I, \boldsymbol{d}_S) - \boldsymbol{g}^S(\boldsymbol{y}_I, \boldsymbol{Q}^{\mathrm{T}}\boldsymbol{d}_S) = \boldsymbol{0} \\ &\left(\sum_{I=1}^{5} (\partial_{\boldsymbol{y}_I} \boldsymbol{g}^S) \widehat{\boldsymbol{y}}_I + (\partial_{\boldsymbol{d}_S} \boldsymbol{g}^S) \widehat{\boldsymbol{d}}_S \right) \boldsymbol{\mu} = \boldsymbol{0} \end{aligned} \tag{64}$$

Similar to the arrangement of the Lagrange multipliers in (12), the totality of the NTS mesh-tying constraints can be arranged in the system vector

$$\boldsymbol{g}(\boldsymbol{q}, \boldsymbol{d}) = \begin{bmatrix} \boldsymbol{g}^{S=1}(\boldsymbol{q}, \boldsymbol{d}) \\ \vdots \\ \boldsymbol{g}^{S=n_{\mathrm{surf}}^{(1)}}(\boldsymbol{q}, \boldsymbol{d}) \end{bmatrix} \tag{65}$$

DOI: 10.1002/nme

such that

$$\sum_{S\in\bar{\omega}^{(1)}} \boldsymbol{\lambda}_S\cdot\boldsymbol{g}^S(\boldsymbol{q},\boldsymbol{d})=\boldsymbol{\lambda}\cdot\boldsymbol{g}(\boldsymbol{q},\boldsymbol{d}) \tag{66}$$

The vector $\boldsymbol{d}\in\mathbb{R}^{3n^{(1)}_{\text{surf}}}$ contains the totality of additional coordinates $\boldsymbol{d}_S\in\mathbb{R}^3$ associated with the nodes $S=1,\ldots,n^{(1)}_{\text{surf}}$ lying on the interface $\Gamma^{(1),\text{h}}$. The modified NTS mesh-tying constraints (64) make possible the design of a specific energy–momentum scheme, as will be shown in Section 6. Moreover, the newly proposed approach developed in the context of the NTS method can be extended to the favorable mortar method in a straightforward way.

5. MORTAR METHOD

The mortar method is based on the mortar integrals (23) instead of the degenerated form (32). This necessitates a segmentation process to perform the evaluation of these integrals, see, for example, Simo *et al.* [38] and Puso [16]. In the context of planar contact problems and linear shape functions,[§] the segmentation process along with the design of frame-indifferent mortar constraints has been outlined in Hesch and Betsch [33]. A similar approach will now be followed in the context of three-dimensional domain decomposition problems.

Consider a typical element $e_2\in\bar{\varepsilon}^{(2)}$, where $\bar{\varepsilon}^{(2)}$ denotes the set of elements on the interface $\Gamma^{(2),\text{h}}$ of an arbitrarily chosen side, referred to as mortar side, with the nodes $\boldsymbol{q}^{(2)}_1,\boldsymbol{q}^{(2)}_2,\boldsymbol{q}^{(2)}_3$ and $\boldsymbol{q}^{(2)}_4$. These nodes are projected orthogonally to each element of the opposing non-mortar side (Figure 3(a)), using Equation (34) to determine the corresponding local coordinate pairs (Figure 3(b))

$$\bar{\boldsymbol{\xi}}^{(1)}=[\bar{\boldsymbol{\xi}}^{(1)}_1,\bar{\boldsymbol{\xi}}^{(1)}_2,\bar{\boldsymbol{\xi}}^{(1)}_3,\bar{\boldsymbol{\xi}}^{(1)}_4] \tag{67}$$

Next a clipping algorithm as proposed in Puso [16] is used to determine the segments (Figure 3(b)), corresponding to each pair of elements $e\in\bar{\varepsilon}^{(1)}$, where $\bar{\varepsilon}^{(1)}$ denotes the set of elements on the interface $\Gamma^{(1),\text{h}}$, and $e_2\in\bar{\varepsilon}^{(2)}$. Each specific segment depends on the corresponding nodal coordinates, which can be collected in the ordered set η^{seg} relevant to the segment at hand

$$\eta^{\text{seg}}=\{\boldsymbol{y}_1,\ldots,\boldsymbol{y}_8\}=\{\boldsymbol{q}^{(1)}_1,\boldsymbol{q}^{(1)}_2,\boldsymbol{q}^{(1)}_3,\boldsymbol{q}^{(1)}_4,\boldsymbol{q}^{(2)}_1,\boldsymbol{q}^{(2)}_2,\boldsymbol{q}^{(2)}_3,\boldsymbol{q}^{(2)}_4\} \tag{68}$$

In this connection, $\boldsymbol{q}^{(1)}_1,\boldsymbol{q}^{(1)}_2,\boldsymbol{q}^{(1)}_3$ and $\boldsymbol{q}^{(1)}_4$ are the nodal position vectors belonging to element e on the non-mortar side. To perform a numerical quadrature of the mortar integrals $(23)_1$ and $(23)_2$, the local coordinates $\boldsymbol{\xi}^{(1)}_{\text{seg}}$ (see Figure 3(c)) of the localized segment as well as the corresponding segment coordinates $\boldsymbol{\xi}^{(2)}_{\text{seg}}$ on the mortar side are needed. For each segment a linear transformation $\boldsymbol{\eta}\rightarrow\boldsymbol{\xi}^{(i),\text{h}}_{\text{seg}}$ of the form

$$\boldsymbol{\xi}^{(i),\text{h}}_{\text{seg}}(\boldsymbol{\eta})=\sum_{K=1}^{3} M^K(\boldsymbol{\eta})\boldsymbol{\xi}^{(i)}_{\text{seg},K} \tag{69}$$

is introduced (Figure 3(d)) where $\boldsymbol{\xi}^{(i)}_{\text{seg},K}$ denotes the vertices of the segment. In accordance with the results of the clipping algorithm, linear triangular shape functions M^K are used. The segment

[§]The treatment of quadratic shape functions is given, e.g. in Hauret and Le Tallec [39] and Puso *et al.* [17].

DOI: 10.1002/nme

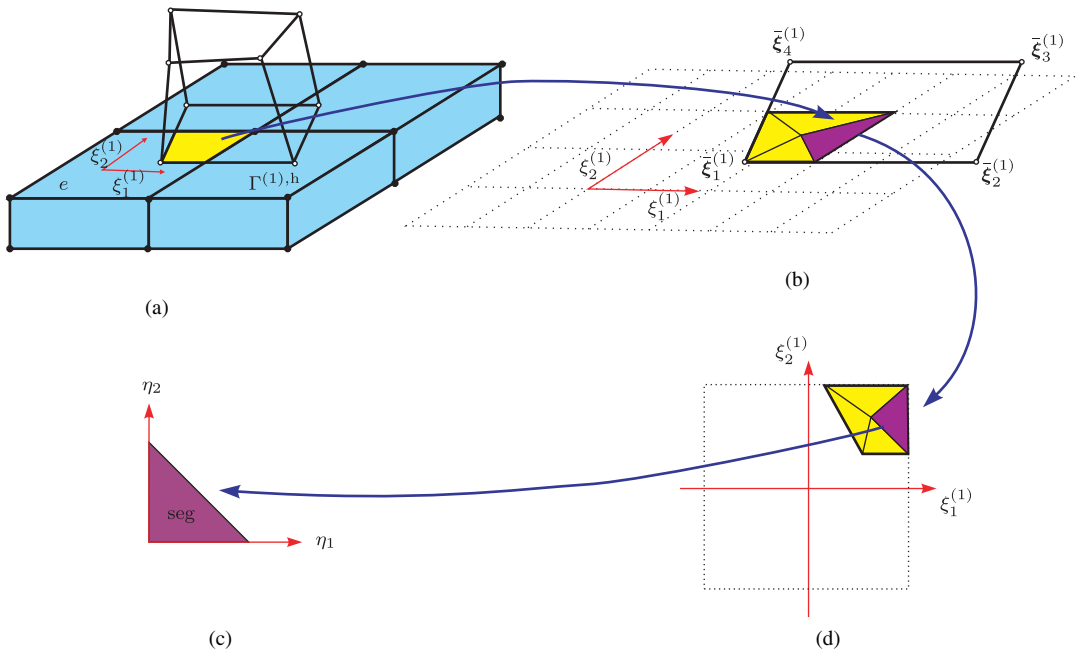

Figure 3. Segmentation process. (a) Representative element e on the non-mortar side $\Gamma^{(1),h}$ and one opposing element e_2 on the mortar side; (b) projection of the nodal points of element e_2 onto the non-mortar side and determination of the relevant segments; (c) location of the segments in the $\xi_1^{(1)}$, $\xi_2^{(1)}$ coordinate system; and (d) coordinate transformation of each segment to a reference triangle with coordinates η_1, η_2.

contributions to the constraints have to be computed by using the approximations (8) and (9), now recast in the form

$$\boldsymbol{t}_{\text{seg}}^{(1),h} = \sum_{\kappa} N^{\kappa}(\boldsymbol{\xi}_{\text{seg}}^{(1),h}(\boldsymbol{\eta}))\boldsymbol{\lambda}_{\kappa} \tag{70}$$

$$\boldsymbol{\varphi}_{\text{seg}}^{(1),h} = \sum_{\beta} N^{\beta}(\boldsymbol{\xi}_{\text{seg}}^{(1),h}(\boldsymbol{\eta}))\boldsymbol{q}_{\beta}^{(1)} \tag{71}$$

$$\boldsymbol{\varphi}_{\text{seg}}^{(2),h} = \sum_{\zeta} N^{\zeta}(\boldsymbol{\xi}_{\text{seg}}^{(2),h}(\boldsymbol{\eta}))\boldsymbol{q}_{\zeta}^{(2)} \tag{72}$$

The mortar integrals for each segment can now be calculated from

$$\begin{aligned} n^{\kappa\beta} &= \int_{\Gamma_{\text{d,seg}}^{(1)}} N^{\kappa}(\boldsymbol{\xi}_{\text{seg}}^{(1),h}(\boldsymbol{\eta}))N^{\beta}(\boldsymbol{\xi}_{\text{seg}}^{(1),h}(\boldsymbol{\eta}))\,\mathrm{d}\Gamma \\ n^{\kappa\zeta} &= \int_{\Gamma_{\text{d,seg}}^{(1)}} N^{\kappa}(\boldsymbol{\xi}_{\text{seg}}^{(1),h}(\boldsymbol{\eta}))N^{\zeta}(\boldsymbol{\xi}_{\text{seg}}^{(2),h}(\boldsymbol{\eta}))\,\mathrm{d}\Gamma \end{aligned} \tag{73}$$

DOI: 10.1002/nme

Furthermore, the Jacobian J_{seg} is required.

$$J_{\text{seg}} = \|\boldsymbol{A}_1(\boldsymbol{\xi}_{\text{seg}}^{(1),\text{h}}(\boldsymbol{\eta})) \times \boldsymbol{A}_2(\boldsymbol{\xi}_{\text{seg}}^{(1),\text{h}}(\boldsymbol{\eta}))\| \det(D\boldsymbol{\xi}(\boldsymbol{\eta})) \tag{74}$$

which has to be evaluated at each quadrature point. Eventually, the mortar integrals on each segment can be written as

$$\begin{aligned} n^{\kappa\beta} &= \int_{\triangle} N^{\kappa}(\boldsymbol{\xi}_{\text{seg}}^{(1),\text{h}}(\boldsymbol{\eta})) N^{\beta}(\boldsymbol{\xi}_{\text{seg}}^{(1),\text{h}}(\boldsymbol{\eta})) J_{\text{seg}}\, \text{d}\eta \\ n^{\kappa\zeta} &= \int_{\triangle} N^{\kappa}(\boldsymbol{\xi}_{\text{seg}}^{(1),\text{h}}(\boldsymbol{\eta})) N^{\zeta}(\boldsymbol{\xi}_{\text{seg}}^{(2),\text{h}}(\boldsymbol{\eta})) J_{\text{seg}}\, \text{d}\eta \end{aligned} \tag{75}$$

The segment contributions of element e to the mortar mesh-tying constraints (26) can be collected in the vector

$$\boldsymbol{\Phi}_{e,\text{seg}}(\boldsymbol{y}_I) = \begin{bmatrix} \boldsymbol{\Phi}_{e,\text{seg}}^{\kappa=1}(\boldsymbol{y}_I) \\ \vdots \\ \boldsymbol{\Phi}_{e,\text{seg}}^{\kappa=4}(\boldsymbol{y}_I) \end{bmatrix} \tag{76}$$

with

$$\boldsymbol{\Phi}_{e,\text{seg}}^{\kappa}(\boldsymbol{y}_I) = \sum_{\beta} n^{\kappa\beta} \boldsymbol{q}_{\beta}^{(1)} - \sum_{\zeta} n^{\kappa\zeta} \boldsymbol{q}_{\zeta}^{(2)} \tag{77}$$

To perform the assembly of the contributions of all elements $e \in \bar{\varepsilon}^{(1)}$ on the non-mortar side, the connection between local and global node numbers is stored in the location array LM, such that $A = \text{LM}(\kappa, e)$, for $A \in \bar{\omega}^{(1)}$, $\kappa \in \{1, \ldots, 4\}$ and $e \in \bar{\varepsilon}^{(1)}$. Accordingly, the mortar constraints follow from

$$\boldsymbol{\Phi}_A \leftarrow \boldsymbol{\Phi}_A + \boldsymbol{\Phi}_e^{\kappa} \tag{78}$$

In the sequel the assembly procedure will be written as[¶]

$$\boldsymbol{\Phi}(\boldsymbol{q}) = \mathop{\mathbf{A}}_{e \in \bar{\varepsilon}^{(1)}} \boldsymbol{\Phi}_e = \mathop{\mathbf{A}}_{e \in \bar{\varepsilon}^{(1)}} \bigcup_{\text{seg}} \boldsymbol{\Phi}_{e,\text{seg}} = \mathop{\mathbf{A}}_{e \in \bar{\varepsilon}^{(1)}} \bigcup_{\text{seg}} \begin{bmatrix} \boldsymbol{\Phi}_{e,\text{seg}}^{\kappa=1} \\ \vdots \\ \boldsymbol{\Phi}_{e,\text{seg}}^{\kappa=4} \end{bmatrix} \tag{79}$$

where $\mathbf{A}$ denotes the standard assembly operator. Note that, similar to the decomposition of the NTS constraints in (36), the segment contributions of the mortar constraints can be recast in the form

$$\boldsymbol{\Phi}_{e,\text{seg}}^{\kappa}(\boldsymbol{y}_I) = \underbrace{\sum_{\beta} n^{\kappa\beta} \boldsymbol{u}_{\beta}^{(1)} - \sum_{\zeta} n^{\kappa\zeta} \boldsymbol{u}_{\zeta}^{(2)}}_{\boldsymbol{\Phi}_{\boldsymbol{u},e,\text{seg}}^{\kappa}} + \underbrace{\sum_{\beta} n^{\kappa\beta} \boldsymbol{X}_{\beta}^{(1)} - \sum_{\zeta} n^{\kappa\zeta} \boldsymbol{X}_{\zeta}^{(2)}}_{\boldsymbol{\Phi}_{\boldsymbol{X},e,\text{seg}}^{\kappa}} \tag{80}$$

[¶]Note that the operation $\mathop{\mathbf{A}}_{e \in \bar{\varepsilon}^{(1)}} \bigcup_{\text{seg}}$ can be done simultaneously within a loop over all segments of the internal boundary.

DOI: 10.1002/nme

5.1. Reformulation of the mortar constraints

Guided by our previous developments in the context of the NTS method (see Section 4), we propose an alternative formulation of the mortar method. Accordingly, we aim at a decomposition of the mortar constraints into normal and tangential components, which can be arranged for each segment contribution. To this end we utilize constant tangential and normal vectors within each segment, defined as follows:

$$\boldsymbol{a}_{\alpha,\mathrm{seg}} = \sum_{B=1}^{4} N^{\kappa}_{,\alpha}(\bar{\boldsymbol{\eta}})\boldsymbol{q}_{\kappa} \quad (\alpha = 1,2) \tag{81}$$

and

$$\boldsymbol{n}_{\mathrm{seg}} = \frac{\boldsymbol{a}_{1,\mathrm{seg}}(\bar{\boldsymbol{\eta}}) \times \boldsymbol{a}_{2,\mathrm{seg}}(\bar{\boldsymbol{\eta}})}{\|\boldsymbol{a}_{1,\mathrm{seg}}(\bar{\boldsymbol{\eta}}) \times \boldsymbol{a}_{2,\mathrm{seg}}(\bar{\boldsymbol{\eta}})\|} \tag{82}$$

Here, $\bar{\boldsymbol{\eta}}$ denotes the local coordinates of the mid-point of the reference triangle. Similar to (39) we propose the following modified form of the mortar segment contributions:

$$\bar{\boldsymbol{\Phi}}^{\kappa}_{e,\mathrm{seg}}(\boldsymbol{y}_I) = \begin{bmatrix} \boldsymbol{\Phi}^{\kappa}_{e,\mathrm{seg}}(\boldsymbol{y}_I)\cdot\boldsymbol{a}_{1,\mathrm{seg}} \\ \boldsymbol{\Phi}^{\kappa}_{e,\mathrm{seg}}(\boldsymbol{y}_I)\cdot\boldsymbol{a}_{2,\mathrm{seg}} \\ \boldsymbol{\Phi}^{\kappa}_{e,\mathrm{seg}}(\boldsymbol{y}_I)\cdot\boldsymbol{n}_{\mathrm{seg}} \end{bmatrix} - \boldsymbol{D}^{\kappa}_{e,\mathrm{seg}} \tag{83}$$

where

$$\boldsymbol{D}^{\kappa}_{e,\mathrm{seg}} = \begin{bmatrix} \boldsymbol{\Phi}^{\kappa}_{e,\mathrm{seg}}(\boldsymbol{X}_I)\cdot\boldsymbol{A}_{1,\mathrm{seg}} \\ \boldsymbol{\Phi}^{\kappa}_{e,\mathrm{seg}}(\boldsymbol{X}_I)\cdot\boldsymbol{A}_{2,\mathrm{seg}} \\ \boldsymbol{\Phi}^{\kappa}_{e,\mathrm{seg}}(\boldsymbol{X}_I)\cdot\boldsymbol{N}_{\mathrm{seg}} \end{bmatrix} \tag{84}$$

Similar to D_S in (39), $\boldsymbol{D}^{\kappa}_{e,\mathrm{seg}}$ can be computed once at problem initialization. In the above equation $\boldsymbol{A}_{1,\mathrm{seg}}$, $\boldsymbol{A}_{2,\mathrm{seg}}$ and $\boldsymbol{N}_{\mathrm{seg}}$ denote the initial values of $\boldsymbol{a}_{1,\mathrm{seg}}$, $\boldsymbol{a}_{2,\mathrm{seg}}$ and $\boldsymbol{n}_{\mathrm{seg}}$.

5.2. Frame-indifference of the modified mortar constraints

For the verification of frame-indifference, we again (see Section 4.2) consider rigid motions of the form

$$\boldsymbol{y}^{\sharp}_I = \boldsymbol{c} + \boldsymbol{Q}\boldsymbol{y}_I \tag{85}$$

In analogy to (43) and (44) it can be easily verified that

$$\boldsymbol{a}^{\sharp}_{\alpha,\mathrm{seg}} = \boldsymbol{Q}\boldsymbol{a}_{\alpha,\mathrm{seg}}, \quad \boldsymbol{n}^{\sharp}_{\mathrm{seg}} = \boldsymbol{Q}\boldsymbol{n}_{\mathrm{seg}} \tag{86}$$

DOI: 10.1002/nme

For the original mortar segment contributions one gets

$$\boldsymbol{\Phi}^{\kappa}_{e,\mathrm{seg}}(\boldsymbol{y}^{\sharp}_{I}) = \sum_{\beta} n^{\kappa\beta}(\boldsymbol{c} + \boldsymbol{Q}\boldsymbol{q}^{(1)}_{\beta}) - \sum_{\zeta} n^{\kappa\zeta}(\boldsymbol{c} + \boldsymbol{Q}\boldsymbol{q}^{(2)}_{\zeta}) = \boldsymbol{Q}\boldsymbol{\Phi}^{\kappa}_{e,\mathrm{seg}}(\boldsymbol{y}_{I}) \tag{87}$$

The confirmation of frame-indifference of the modified mortar segment contributions is now straightforward

$$\begin{aligned}
\bar{\boldsymbol{\Phi}}^{\kappa}_{e,\mathrm{seg}}(\boldsymbol{y}^{\sharp}_{I}) &= \begin{bmatrix} \boldsymbol{\Phi}^{\kappa}_{e,\mathrm{seg}}(\boldsymbol{y}^{\sharp}_{I}) \cdot \boldsymbol{a}^{\sharp}_{1,\mathrm{seg}} \\ \boldsymbol{\Phi}^{\kappa}_{e,\mathrm{seg}}(\boldsymbol{y}^{\sharp}_{I}) \cdot \boldsymbol{a}^{\sharp}_{2,\mathrm{seg}} \\ \boldsymbol{\Phi}^{\kappa}_{e,\mathrm{seg}}(\boldsymbol{y}^{\sharp}_{I}) \cdot \boldsymbol{n}^{\sharp}_{\mathrm{seg}} \end{bmatrix} - \boldsymbol{D}^{\kappa}_{e,\mathrm{seg}} \\
&= \begin{bmatrix} \boldsymbol{\Phi}^{\kappa}_{e,\mathrm{seg}}(\boldsymbol{y}_{I}) \cdot \boldsymbol{Q}^{\mathrm{T}}\boldsymbol{Q}\boldsymbol{a}_{1,\mathrm{seg}} \\ \boldsymbol{\Phi}^{\kappa}_{e,\mathrm{seg}}(\boldsymbol{y}_{I}) \cdot \boldsymbol{Q}^{\mathrm{T}}\boldsymbol{Q}\boldsymbol{a}_{2,\mathrm{seg}} \\ \boldsymbol{\Phi}^{\kappa}_{e,\mathrm{seg}}(\boldsymbol{y}_{I}) \cdot \boldsymbol{Q}^{\mathrm{T}}\boldsymbol{Q}\boldsymbol{n}_{\mathrm{seg}} \end{bmatrix} - \boldsymbol{D}^{\kappa}_{e,\mathrm{seg}} \\
&= \bar{\boldsymbol{\Phi}}^{\kappa}_{e,\mathrm{seg}}(\boldsymbol{y}_{I})
\end{aligned} \tag{88}$$

The frame-indifference of the modified mortar segment contributions implies translational and rotational invariances, i.e. $\bar{\boldsymbol{\Phi}}^{\kappa}_{e,\mathrm{seg}}(\boldsymbol{y}_{I} + \varepsilon\boldsymbol{\mu}) = \bar{\boldsymbol{\Phi}}^{\kappa}_{e,\mathrm{seg}}(\boldsymbol{y}_{I})$ and $\bar{\boldsymbol{\Phi}}^{\kappa}_{e,\mathrm{seg}}(\exp(\varepsilon\widehat{\boldsymbol{\mu}})\boldsymbol{y}_{I}) = \bar{\boldsymbol{\Phi}}^{\kappa}_{e,\mathrm{seg}}(\boldsymbol{y}_{I})$ for arbitrary $\varepsilon \in \mathbb{R}$. It is important to realize that the frame-indifference of the modified mortar segment contributions transfers to the corresponding mortar constraints by applying the assembly procedure as outlined above. With regard to (49) and (50), conservation of linear and angular momentums follows immediately from the property of frame-indifference. Furthermore, with regard to the sets defined in (51) and (52) each segment contribution of the mortar constraints depends on the set of invariants $\mathbb{S}(\eta^{\mathrm{seg}}) \cup \mathbb{T}(\eta^{\mathrm{seg}})$. Analogous to (51) and (52), $\mathbb{S}(\eta^{\mathrm{seg}})$ and $\mathbb{T}(\eta^{\mathrm{seg}})$ denote the set of quadratic and cubic functions of the nodal position vectors in η^{seg}.

5.3. Augmented coordinates

Similar to Section 4.3, we introduce additional coordinates $\boldsymbol{d}_{\mathrm{seg}} \in \mathbb{R}^3$ for each segment. Accordingly, the coordinate augmentation yields the extended set of vectors

$$\eta^{\mathrm{seg,aug}} = \{\boldsymbol{q}^{(1)}_{1}, \boldsymbol{q}^{(1)}_{2}, \boldsymbol{q}^{(1)}_{3}, \boldsymbol{q}^{(1)}_{4}, \boldsymbol{q}^{(2)}_{1}, \boldsymbol{q}^{(2)}_{2}, \boldsymbol{q}^{(2)}_{3}, \boldsymbol{q}^{(2)}_{4}, \boldsymbol{d}_{\mathrm{seg}}\} \tag{89}$$

along with additional constraint functions of the form

$$\boldsymbol{\Phi}^{\mathrm{aug}}_{\mathrm{seg}}(\boldsymbol{y}_{I}, \boldsymbol{d}_{\mathrm{seg}}) = \begin{bmatrix} \boldsymbol{d}_{\mathrm{seg}} \cdot \boldsymbol{a}_{1,\mathrm{seg}} \\ \boldsymbol{d}_{\mathrm{seg}} \cdot \boldsymbol{a}_{2,\mathrm{seg}} \\ \frac{1}{2}(\boldsymbol{d}_{\mathrm{seg}} \cdot \boldsymbol{d}_{\mathrm{seg}} - 1) \end{bmatrix} \tag{90}$$

As for the augmentation constraints of the NTS element, it is obvious that the properties (55), (56) and (57) remain unchanged in the present case. In analogy to (60), the modified mortar segment

DOI: 10.1002/nme

contributions can now be written as quadratic functions of the vectors in $\eta^{\mathrm{seg,aug}}$, leading to

$$\tilde{\boldsymbol{\Phi}}^{\kappa}_{e,\mathrm{seg}}(\boldsymbol{y}_I,\boldsymbol{d}_{\mathrm{seg}})=\begin{bmatrix}\boldsymbol{\Phi}^{\kappa}_{e,\mathrm{seg}}(\boldsymbol{y}_I)\cdot\boldsymbol{a}_{1,\mathrm{seg}}\\ \boldsymbol{\Phi}^{\kappa}_{e,\mathrm{seg}}(\boldsymbol{y}_I)\cdot\boldsymbol{a}_{2,\mathrm{seg}}\\ \boldsymbol{\Phi}^{\kappa}_{e,\mathrm{seg}}(\boldsymbol{y}_I)\cdot\boldsymbol{d}_{\mathrm{seg}}\end{bmatrix}-\boldsymbol{D}^{\kappa}_{e,\mathrm{seg}} \tag{91}$$

Analogous to (61) and (63) we obtain

$$\tilde{\boldsymbol{\Phi}}^{\kappa}_{e,\mathrm{seg}}(\boldsymbol{y}^{\sharp}_I,\boldsymbol{d}_{\mathrm{seg}})=\tilde{\boldsymbol{\Phi}}^{\kappa}_{e,\mathrm{seg}}(\boldsymbol{y}_I,\boldsymbol{Q}^{\mathrm{T}}\boldsymbol{d}_{\mathrm{seg}})=\begin{bmatrix}\boldsymbol{\Phi}^{\kappa}_{e,\mathrm{seg}}(\boldsymbol{y}_I)\cdot\boldsymbol{a}_{1,\mathrm{seg}}\\ \boldsymbol{\Phi}^{\kappa}_{e,\mathrm{seg}}(\boldsymbol{y}_I)\cdot\boldsymbol{a}_{2,\mathrm{seg}}\\ \boldsymbol{\Phi}^{\kappa}_{e,\mathrm{seg}}(\boldsymbol{y}_I)\cdot\boldsymbol{Q}^{\mathrm{T}}\boldsymbol{d}_{\mathrm{seg}}\end{bmatrix}-\boldsymbol{D}^{\kappa}_{e,\mathrm{seg}} \tag{92}$$

which implies, similar to (62),

$$\left(\sum_{I=1}^{8}\partial_{\boldsymbol{y}_I}\tilde{\boldsymbol{\Phi}}^{\kappa}_{e,\mathrm{seg}}\hat{\boldsymbol{y}}_I+\partial_{\boldsymbol{d}_{\mathrm{seg}}}\tilde{\boldsymbol{\Phi}}^{\kappa}_{e,\mathrm{seg}}\hat{\boldsymbol{d}}_{\mathrm{seg}}\right)\boldsymbol{\mu}=0 \tag{93}$$

With regard to Section 5, the assembly of the modified mortar segment contributions yields the modified mortar constraints. In addition to that, due to the augmentation procedure, the constraints (90) pertaining to each segment have to be taken into account. To summarize, we arrive at the vector of constraint functions

$$\boldsymbol{g}(\boldsymbol{q},\boldsymbol{d})=\begin{bmatrix}\mathop{\mathbf{A}}_{e\in\bar{\varepsilon}^{(1)}}\bigcup_{\mathrm{seg}}\begin{bmatrix}\tilde{\boldsymbol{\Phi}}^{\kappa=1}_{e,\mathrm{seg}}\\ \vdots\\ \tilde{\boldsymbol{\Phi}}^{\kappa=4}_{e,\mathrm{seg}}\end{bmatrix}\\ \begin{bmatrix}\boldsymbol{\Phi}^{\mathrm{aug}}_{\mathrm{seg}=1}\\ \vdots\\ \boldsymbol{\Phi}^{\mathrm{aug}}_{\mathrm{seg}=n_{\mathrm{seg}}}\end{bmatrix}\end{bmatrix} \tag{94}$$

where n_{seg} denotes the total number of segments on the interface. We emphasis again that the frame-indifference of the mortar segment contributions is not affected by the assembly procedure.

6. EQUATIONS OF MOTION

The present finite-dimensional mechanical system subject to the mesh-tying constraints can be associated with an augmented Lagrangian of the form

$$L_{\lambda}=\tfrac{1}{2}\dot{\boldsymbol{q}}\cdot\boldsymbol{M}\dot{\boldsymbol{q}}-V(\boldsymbol{q})-\boldsymbol{\lambda}\cdot\boldsymbol{g}(\boldsymbol{q},\boldsymbol{d}) \tag{95}$$

where $\boldsymbol{q}$ contains the nodal coordinates resulting from the space discretization, and $\boldsymbol{d}$ contains the additional coordinates due to the coordinate augmentation described above. Moreover, $\boldsymbol{g}(\boldsymbol{q},\boldsymbol{d})$ is

DOI: 10.1002/nme

the vector of constraint functions. The equations of motion of the constrained semi-discrete system under consideration can now be written as

$$\begin{aligned} \boldsymbol{M}\ddot{\boldsymbol{q}} &= -\nabla V(\boldsymbol{q}) - (\mathrm{D}_1 \boldsymbol{g}(\boldsymbol{q},\boldsymbol{d}))^{\mathrm{T}} \boldsymbol{\lambda} \\ \boldsymbol{0} &= (\mathrm{D}_2 \boldsymbol{g}(\boldsymbol{q},\boldsymbol{d}))^{\mathrm{T}} \boldsymbol{\lambda} \\ \boldsymbol{0} &= \boldsymbol{g}(\boldsymbol{q},\boldsymbol{d}) \end{aligned} \tag{96}$$

Here, $\mathrm{D}_1 g(\bullet,\bullet)$ and $\mathrm{D}_2 g(\bullet,\bullet)$ denote the derivative of $g(\bullet,\bullet)$ with respect to the first and the second slots, respectively. The geometric constraints in $(96)_3$ imply the consistency condition $\mathrm{d}\boldsymbol{g}/\mathrm{d}t = \boldsymbol{0}$, leading to the constraints on the velocity level

$$(\mathrm{D}_1 \boldsymbol{g}(\boldsymbol{q},\boldsymbol{d}))\dot{\boldsymbol{q}} + (\mathrm{D}_2 \boldsymbol{g}(\boldsymbol{q},\boldsymbol{d}))\dot{\boldsymbol{d}} = \boldsymbol{0} \tag{97}$$

It has been shown in the above treatment of the mesh-tying constraints that the following property holds for both the NTS method and the mortar method:

$$\sum_{A=1} (\partial_{\boldsymbol{q}_A} \boldsymbol{g}(\boldsymbol{q},\boldsymbol{d}))\widehat{\boldsymbol{q}}_A \boldsymbol{\mu} + \sum_{S=1} (\partial_{\boldsymbol{d}_S} \boldsymbol{g}(\boldsymbol{q},\boldsymbol{d}))\widehat{\boldsymbol{d}}_S \boldsymbol{\mu} = \boldsymbol{0} \tag{98}$$

In the case of the NTS method $S = 1, \ldots, n_{\mathrm{surf}}^{(1)}$, while for the mortar method $S = \mathrm{seg} = 1, \ldots, n_{\mathrm{seg}}$. The total angular momentum of the semi-discrete system at hand is given by

$$\boldsymbol{J} = \sum_{A,B} M^{AB} \boldsymbol{q}_A \times \dot{\boldsymbol{q}}_B \tag{99}$$

We next verify conservation of angular momentum. For simplicity of exposition assume that $V = 0$. Then calculate

$$\begin{aligned} \boldsymbol{\mu} \cdot \frac{\mathrm{d}}{\mathrm{d}t} \boldsymbol{J} &= \boldsymbol{\mu} \cdot \sum_{A,B} M^{AB} \boldsymbol{q}_A \times \ddot{\boldsymbol{q}}_B \\ &= -\boldsymbol{\mu} \cdot \sum_{A} \boldsymbol{q}_A \times (\partial_{\boldsymbol{q}_A} \boldsymbol{g}(\boldsymbol{q},\boldsymbol{d}))^{\mathrm{T}} \boldsymbol{\lambda} \\ &= -\boldsymbol{\mu} \cdot \sum_{A} \widehat{\boldsymbol{q}}_A (\partial_{\boldsymbol{q}_A} \boldsymbol{g}(\boldsymbol{q},\boldsymbol{d}))^{\mathrm{T}} \boldsymbol{\lambda} \\ &= \boldsymbol{\lambda} \cdot \sum_{A} (\partial_{\boldsymbol{q}_A} \boldsymbol{g}(\boldsymbol{q},\boldsymbol{d}))\widehat{\boldsymbol{q}}_A \boldsymbol{\mu} \\ &= -\boldsymbol{\lambda} \cdot \sum_{S} (\partial_{\boldsymbol{d}_S} \boldsymbol{g}(\boldsymbol{q},\boldsymbol{d}))\widehat{\boldsymbol{d}}_S \boldsymbol{\mu} \\ &= \boldsymbol{\mu} \cdot \sum_{S} \widehat{\boldsymbol{d}}_S (\partial_{\boldsymbol{d}_S} \boldsymbol{g}(\boldsymbol{q},\boldsymbol{d}))^{\mathrm{T}} \boldsymbol{\lambda} \\ &= 0 \end{aligned} \tag{100}$$

DOI: 10.1002/nme

which holds for arbitrary $\boldsymbol{\mu}\in\mathbb{R}^3$. Note that in the above manipulations use has been made of (98) and $(96)_2$. To verify conservation of energy, scalar multiply $(96)_1$ by $\dot{\boldsymbol{q}}$ to get

$$\begin{aligned}
\dot{\boldsymbol{q}}\cdot\boldsymbol{M}\ddot{\boldsymbol{q}}+\nabla V(\boldsymbol{q})\cdot\dot{\boldsymbol{q}}+\dot{\boldsymbol{q}}\cdot(\mathrm{D}_1\boldsymbol{g}(\boldsymbol{q},\boldsymbol{d}))^{\mathrm{T}}\boldsymbol{\lambda}&=0\\
\frac{\mathrm{d}}{\mathrm{d}t}\left(\frac{1}{2}\dot{\boldsymbol{q}}\cdot\boldsymbol{M}\dot{\boldsymbol{q}}\right)+\frac{\mathrm{d}}{\mathrm{d}t}V(\boldsymbol{q})+\boldsymbol{\lambda}\cdot(\mathrm{D}_1\boldsymbol{g}(\boldsymbol{q},\boldsymbol{d}))\dot{\boldsymbol{q}}&=0\\
\frac{\mathrm{d}}{\mathrm{d}t}(T+V)-\boldsymbol{\lambda}\cdot(\mathrm{D}_2\boldsymbol{g}(\boldsymbol{q},\boldsymbol{d}))\dot{\boldsymbol{d}}&=0\\
\frac{\mathrm{d}}{\mathrm{d}t}(T+V)-\dot{\boldsymbol{d}}\cdot(\mathrm{D}_2\boldsymbol{g}(\boldsymbol{q},\boldsymbol{d}))^{\mathrm{T}}\boldsymbol{\lambda}&=0\\
\frac{\mathrm{d}}{\mathrm{d}t}(T+V)&=0
\end{aligned}\tag{101}$$

where use has been made of (97) and $(96)_2$.

6.1. Time discretization

We next deal with the time discretization of the DAEs (96). Similar to the energy–momentum schemes for constrained mechanical systems developed by Gonzalez [22] and Betsch and Steinmann [24], we consider the following time-stepping scheme:

$$\begin{aligned}
\boldsymbol{q}_{n+1}-\boldsymbol{q}_n&=\Delta t\boldsymbol{v}_{n+1/2}\\
\boldsymbol{M}(\boldsymbol{v}_{n+1}-\boldsymbol{v}_n)&=-\Delta t\overline{\nabla}V(\boldsymbol{q}_n,\boldsymbol{q}_{n+1})-\Delta t(\mathrm{D}_1\boldsymbol{g}(\boldsymbol{q}_{n+1/2},\boldsymbol{d}_{n+1/2}))^{\mathrm{T}}\boldsymbol{\lambda}_{n+1}\\
\boldsymbol{0}&=\mathrm{D}_2(\boldsymbol{g}(\boldsymbol{q}_{n+1/2},\boldsymbol{d}_{n+1/2}))^{\mathrm{T}}\boldsymbol{\lambda}_{n+1}\\
\boldsymbol{0}&=\boldsymbol{g}(\boldsymbol{q}_{n+1},\boldsymbol{d}_{n+1})
\end{aligned}\tag{102}$$

In this connection, $\boldsymbol{q}_n$ and $\boldsymbol{d}_n$ are consistent initial values per time step, which have to satisfy $\boldsymbol{g}(\boldsymbol{q}_n,\boldsymbol{d}_n)=\boldsymbol{0}$. Moreover, $(\bullet)_{n+1/2}=[(\bullet)_n+(\bullet)_{n+1}]/2$ denotes the mid-point value of the quantity $(\bullet)$, Δt is the time step and $\overline{\nabla}V(\boldsymbol{q}_n,\boldsymbol{q}_{n+1})$ denotes a discrete gradient of the potential function in the sense of Gonzalez [21]. The scheme (102) determines $\boldsymbol{q}_{n+1}$, $\boldsymbol{v}_{n+1}$ and $\boldsymbol{\lambda}_{n+1}$. For later use we remark that property (98) implies that

$$\sum_{A=1}(\partial_{\boldsymbol{q}_A}\boldsymbol{g}(\boldsymbol{q}_{n+1/2},\boldsymbol{d}_{n+1/2}))\widehat{\boldsymbol{q}}_{A_{n+1/2}}\boldsymbol{\mu}+\sum_{S}(\partial_{\boldsymbol{d}_S}\boldsymbol{g}(\boldsymbol{q}_{n+1/2},\boldsymbol{d}_{n+1/2}))\widehat{\boldsymbol{d}}_{S_{n+1/2}}\boldsymbol{\mu}=\boldsymbol{0}\tag{103}$$

Furthermore, due to the fact that the constraint function $\boldsymbol{g}(\boldsymbol{q},\boldsymbol{d})$ is quadratic in $\boldsymbol{q}$ and $\boldsymbol{d}$, the following property is satisfied:

$$\begin{aligned}
&(\mathrm{D}_1\boldsymbol{g}(\boldsymbol{q}_{n+1/2},\boldsymbol{d}_{n+1/2}))(\boldsymbol{q}_{n+1}-\boldsymbol{q}_n)+(\mathrm{D}_2\boldsymbol{g}(\boldsymbol{q}_{n+1/2},\boldsymbol{d}_{n+1/2}))(\boldsymbol{d}_{n+1}-\boldsymbol{d}_n)\\
&\quad=\boldsymbol{g}(\boldsymbol{q}_{n+1},\boldsymbol{d}_{n+1})-\boldsymbol{g}(\boldsymbol{q}_n,\boldsymbol{d}_n)=\boldsymbol{0}
\end{aligned}\tag{104}$$

where $(102)_4$ has been accounted for. Note that the last equation can be viewed as discrete counterpart of the velocity constraints (97). We next verify algorithmic conservation of angular

DOI: 10.1002/nme

momentum (again assuming that $V=0$). Since the angular momentum map $\boldsymbol{J}(\boldsymbol{q},\boldsymbol{v})$, (99), is a quadratic function of $(\boldsymbol{q},\boldsymbol{v})$, we have

$$\begin{aligned}
&\boldsymbol{J}(\boldsymbol{q}_{n+1},\boldsymbol{v}_{n+1})-\boldsymbol{J}(\boldsymbol{q}_n,\boldsymbol{v}_n)\\
&=(\mathrm{D}_1\boldsymbol{J}(\boldsymbol{q}_{n+1/2},\boldsymbol{v}_{n+1/2}))(\boldsymbol{q}_{n+1}-\boldsymbol{q}_n)+(\mathrm{D}_2\boldsymbol{J}(\boldsymbol{q}_{n+1/2},\boldsymbol{v}_{n+1/2}))(\boldsymbol{v}_{n+1}-\boldsymbol{v}_n)\\
&=-\sum_{A,B}M^{AB}\boldsymbol{v}_{B_{n+1/2}}\times(\boldsymbol{q}_{A_{n+1}}-\boldsymbol{q}_{A_n})+\sum_{A,B}M^{AB}\boldsymbol{q}_{B_{n+1/2}}\times(\boldsymbol{v}_{A_{n+1}}-\boldsymbol{v}_{A_n})
\end{aligned}\tag{105}$$

Scalar multiplying the last equation by $\boldsymbol{\mu}$, and subsequently substituting from $(102)_1$ and $(102)_2$ yields

$$\begin{aligned}
\boldsymbol{\mu}\cdot(\boldsymbol{J}_{n+1}-\boldsymbol{J}_n)&=-\Delta t\,\boldsymbol{\mu}\cdot\sum_B\boldsymbol{q}_{B_{n+1/2}}\times(\partial_{\boldsymbol{q}_B}\boldsymbol{g}(\boldsymbol{q}_{n+1/2},\boldsymbol{d}_{n+1/2}))^{\mathrm{T}}\boldsymbol{\lambda}_{n+1}\\
&=\Delta t\,\boldsymbol{\lambda}_{n+1}\cdot\sum_B(\partial_{\boldsymbol{q}_B}\boldsymbol{g}(\boldsymbol{q}_{n+1/2},\boldsymbol{d}_{n+1/2}))\widehat{\boldsymbol{q}}_{B_{n+1/2}}\boldsymbol{\mu}\\
&=-\Delta t\,\boldsymbol{\lambda}_{n+1}\cdot\sum_S(\partial_{\boldsymbol{d}_S}\boldsymbol{g}(\boldsymbol{q}_{n+1/2},\boldsymbol{d}_{n+1/2}))\widehat{\boldsymbol{d}}_{S_{n+1/2}}\boldsymbol{\mu}\\
&=\Delta t\,\boldsymbol{\mu}\cdot\sum_S\widehat{\boldsymbol{q}}_{S_{n+1/2}}(\partial_{\boldsymbol{d}_S}\boldsymbol{g}(\boldsymbol{q}_{n+1/2},\boldsymbol{d}_{n+1/2}))^{\mathrm{T}}\boldsymbol{\lambda}_{n+1}\\
&=0
\end{aligned}\tag{106}$$

where use has been made of (103) and $(102)_3$. Eventually, we verify algorithmic conservation of energy. Scalar multiplying $(102)_2$ by $\boldsymbol{v}_{n+1/2}$, taking into account $(102)_1$, yields

$$\begin{aligned}
\boldsymbol{v}_{n+1/2}\cdot\boldsymbol{M}(\boldsymbol{v}_{n+1}-\boldsymbol{v}_n)&=-\overline{\nabla}V(\boldsymbol{q}_n,\boldsymbol{q}_{n+1})\cdot(\boldsymbol{q}_{n+1}-\boldsymbol{q}_n)\\
&\quad-(\boldsymbol{q}_{n+1}-\boldsymbol{q}_n)\cdot(\mathrm{D}_1\boldsymbol{g}(\boldsymbol{q}_{n+1/2},\boldsymbol{d}_{n+1/2}))^{\mathrm{T}}\boldsymbol{\lambda}_{n+1}
\end{aligned}\tag{107}$$

The last equation can be recast in the form

$$\begin{aligned}
\tfrac{1}{2}\boldsymbol{v}_{n+1}\cdot\boldsymbol{M}\boldsymbol{v}_{n+1}-\tfrac{1}{2}\boldsymbol{v}_n\cdot\boldsymbol{M}\boldsymbol{v}_n&=-[V(\boldsymbol{q}_{n+1})-V(\boldsymbol{q}_n)]\\
&\quad+\boldsymbol{\lambda}_{n+1}\cdot(\mathrm{D}_1\boldsymbol{g}(\boldsymbol{q}_{n+1/2},\boldsymbol{d}_{n+1/2}))(\boldsymbol{q}_{n+1}-\boldsymbol{q}_n)
\end{aligned}\tag{108}$$

where the directionality property of the discrete derivative (see Gonzalez [21]) has been employed. Introducing the total energy function

$$E(\boldsymbol{q},\boldsymbol{v})=\tfrac{1}{2}\boldsymbol{v}\cdot\boldsymbol{M}\boldsymbol{v}+V(\boldsymbol{q})\tag{109}$$

DOI: 10.1002/nme

and taking into account (104), Equation (108) can be rewritten as

$$\begin{aligned} E(\boldsymbol{q}_{n+1},\boldsymbol{v}_{n+1})-E(\boldsymbol{q}_n,\boldsymbol{v}_n) &= -\boldsymbol{\lambda}_{n+1}\cdot(\mathrm{D}_2\boldsymbol{g}(\boldsymbol{q}_{n+\frac{1}{2}},\boldsymbol{d}_{n+\frac{1}{2}}))(\boldsymbol{d}_{n+1}-\boldsymbol{d}_n) \\ &= -(\boldsymbol{d}_{n+1}-\boldsymbol{d}_n)\cdot(\mathrm{D}_2\boldsymbol{g}(\boldsymbol{q}_{n+1/2},\boldsymbol{d}_{n+1/2}))^{\mathrm{T}}\boldsymbol{\lambda}_{n+1} \\ &= \mathbf{0} \end{aligned} \tag{110}$$

where use has been made of $(102)_3$.

7. NUMERICAL EXAMPLES

We next present three representative examples dealing with domain decomposition problems. Concerning the numerical evaluation of the mortar integrals, four Gauss points have been used per segment. As has been outlined in Section 6.1, the notion of a discrete derivative is applied to the potential energy function (17). In particular, $\overline{\nabla} V^{(i),\mathrm{int}}(\boldsymbol{q}_n^{(i)},\boldsymbol{q}_{n+1}^{(i)})$ is calculated as proposed by Gonzalez [40], see also Betsch and Hesch [32, Section 3.4].

7.1. Flying L-shaped block

The first example deals with a continuum body that assumes the form of an L-shaped block in the stress-free initial configuration (see Figure 4). The block is divided into two parts, which are independently meshed. In particular, the larger part consists of 648 elements ($18\times6\times6$), while the smaller small part comprises 1000 elements ($10\times10\times10$). Consequently, the two meshes do not conform on the interface. To couple the two semi-discrete parts, the mortar mesh-tying constraints (94) are used. The model consists of 6786 degrees of freedom, the segmentation process generates 801 segments for 399 constraints. Therefore, 2403 additional constraints for the augmentation are needed. Hyperelastic constitutive behavior is assumed to be governed by a compressible Neo-Hooke material with associated stored energy function

$$W(\boldsymbol{C})=\frac{\mu}{2}[\mathrm{tr}(\boldsymbol{C})-3]+\frac{\lambda}{2}(\ln(J))^2-\mu\ln(J) \tag{111}$$

where $J=\sqrt{\det(\boldsymbol{C})}$. First, a quasi-rigid material behavior is investigated. The corresponding material constants are assumed to take the values $\lambda=300\,000$, $\mu=75\,000$ and $\rho=100$, where λ and μ denote Lamé parameters and ρ is the density. To initiate the motion, external pressure loads are acting on the block for $0\leqslant t\leqslant0.5$, see Figure 4. Figure 5 indicates the sinusoidal pressure load. In the simulations documented below a constant time step size of $\Delta t=0.01$ has been used. To illustrate the resulting motion of the L-shaped block, snapshots at successive points in time are depicted in Figure 6. For $t>0.5$ the present example can be classified as autonomous Hamiltonian system with symmetry. Accordingly, the total energy, angular momentum and linear momentum are conserved quantities for $t>0.5$. The present energy–momentum scheme does indeed conserve these quantities. This can be observed from Figures 7–9.

DOI: 10.1002/nme

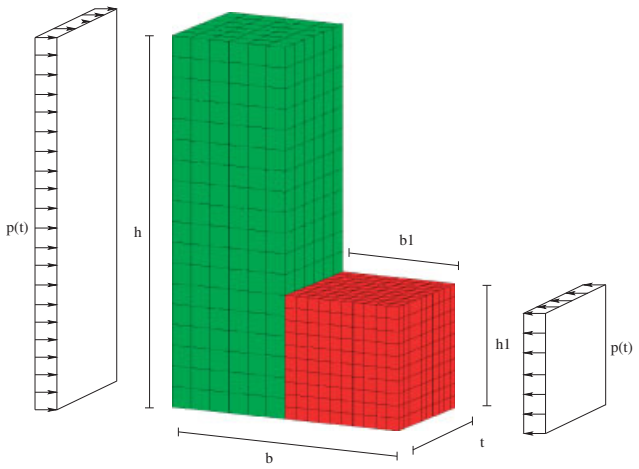

Figure 4. Initial mesh configuration of the L-shaped block.

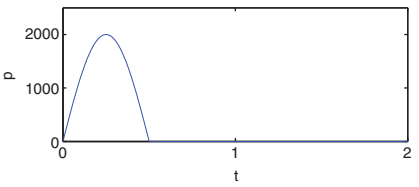

Figure 5. Time history of the pressure load.

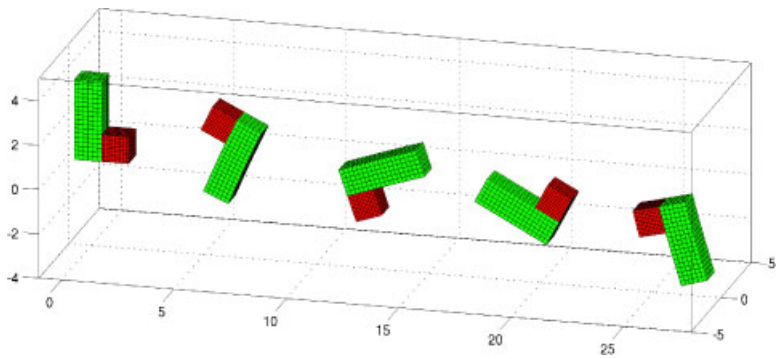

Figure 6. Quasi-rigid motion: snapshots of the motion at $t = 0, 2.5, 5, 7.5, 10$.

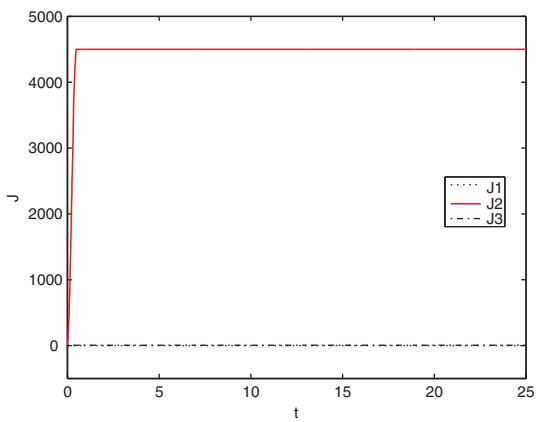

Figure 7. Total angular momentum.

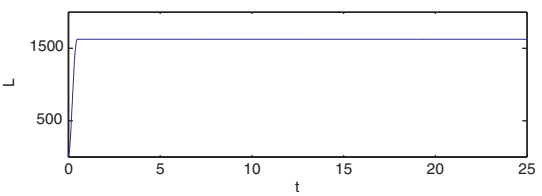

Figure 8. Total linear momentum.

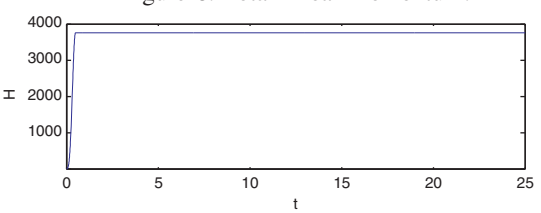

Figure 9. Total energy.

DOI: 10.1002/nme

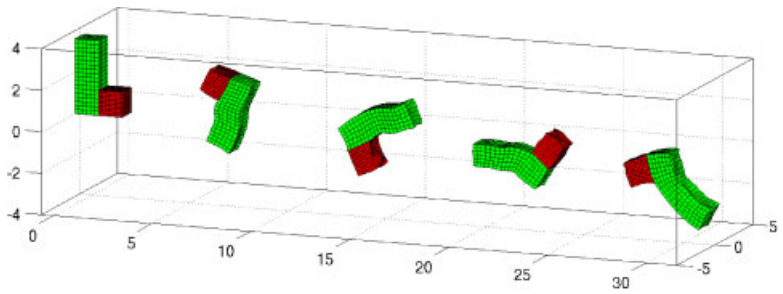

Figure 10. Large strain motion: sequence of deformed configurations at $t=0, 2.5, 5, 7.5, 10$.

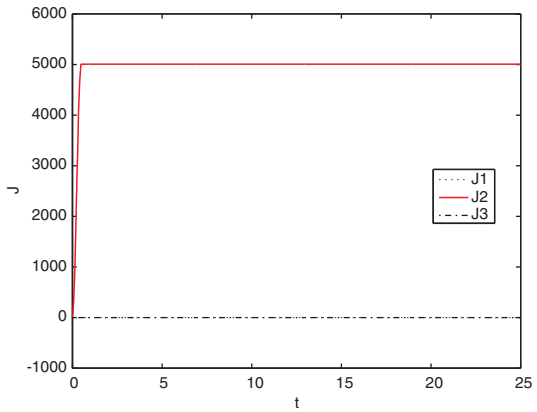

Figure 11. Total angular momentum.

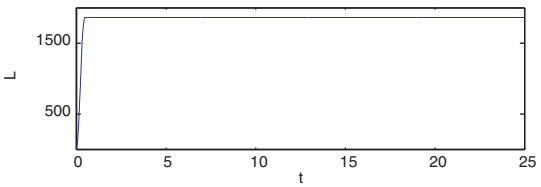

Figure 12. Total linear momentum.

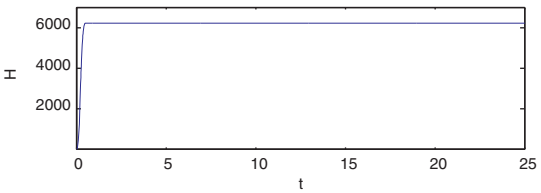

Figure 13. Total energy.

Next, a soft material behavior is modelled by setting the material constants to $\lambda=14285$ and $\mu=3571$. A sequence of deformed configurations is shown in Figure 10. In the simulations a time step size of $\Delta t=0.01$ has been used. Again the present energy–momentum scheme guarantees a stable simulation due to its algorithmic conservation properties. For $t>0.5$, conservation of the total angular momentum, linear momentum and energy can be observed from Figures 11–13.

7.2. Patch test

This static example demonstrates the advantage of the mortar method over the NTS method. As shown in Figure 14, two independently meshed blocks are tied together via a highly curved and non-conforming interface. The upper block consists of 180 ($6\times6\times5$) elements, while the lower block comprises 512 ($8\times8\times8$) elements. A constant pressure field is acting in vertical direction on the upper surface (see Figure 14). The lower left corner is fixed in space, while all other nodes of the bottom surface are fixed in vertical direction. As in the last example compressible Neo-Hooke material is used with the Poisson ratio of $\nu=0.3$ and Young's modulus of $E=10000$. The load has been increased in 15 increments up to $p=7500$. The well-known failure of the NTS

DOI: 10.1002/nme

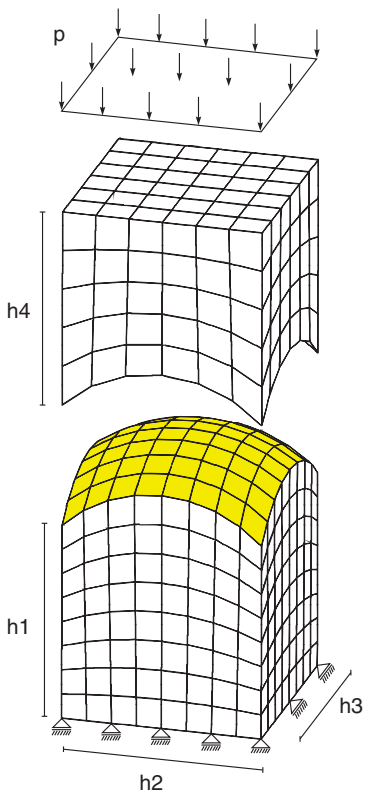

Figure 14. Initial mesh configuration for the patch test.

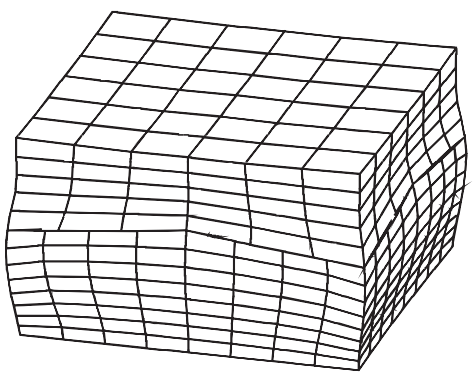

Figure 15. NTS method: deformed configuration (p=7500).

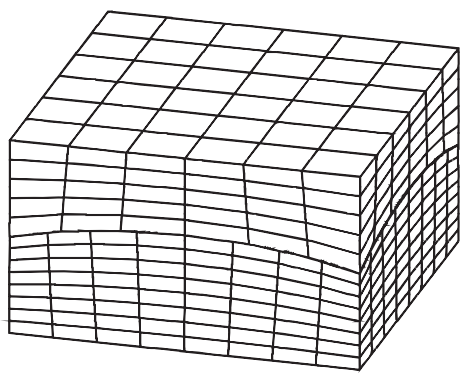

Figure 16. Mortar method: deformed configuration (p=7500).

DOI: 10.1002/nme

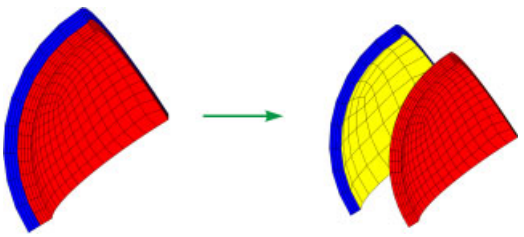

Figure 17. Octant-sphere: two parts that have been independently meshed.

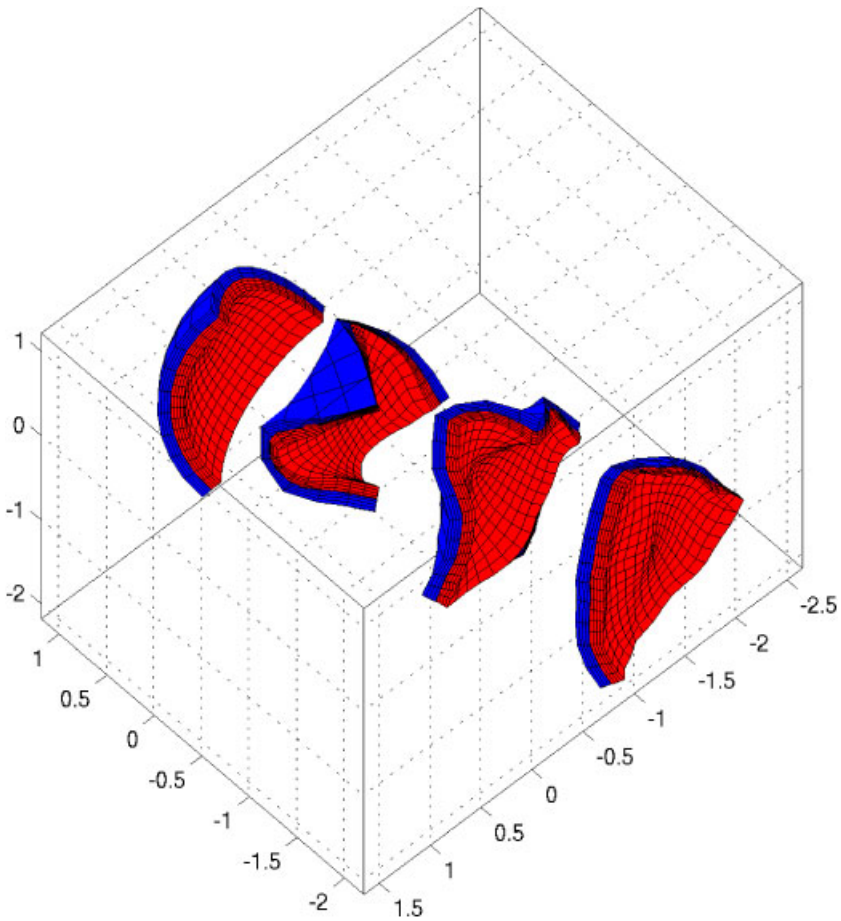

Figure 18. Octant-sphere: sequence of deformed configurations corresponding to $t = 0, 1.66, 3.33, 5$.

method to pass the patch test is reflected by a non-physical deformation of the block depicted in Figure 15. In contrast to that, the mortar method facilitates homogeneous states of stress. As can be observed from Figure 16, the planar faces of the block are still planar even for $p = 7500$, leading to a compression of the block about 55%.

DOI: 10.1002/nme

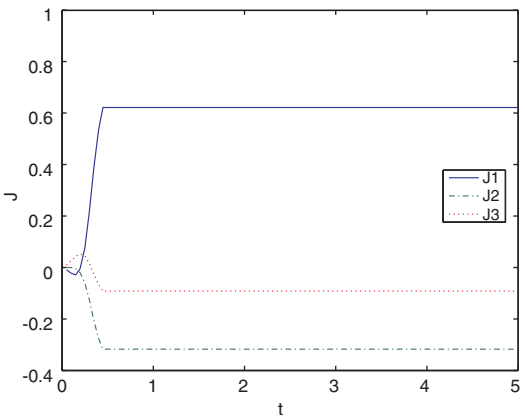

Figure 19. Total angular momentum ($\Delta t = 0.05$).

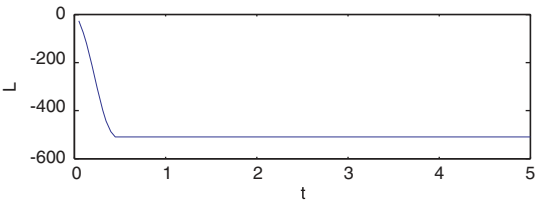

Figure 20. Total linear momentum ($\Delta t = 0.05$).

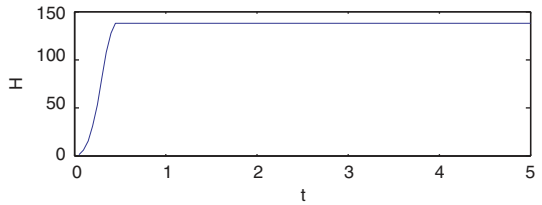

Figure 21. Total energy ($\Delta t = 0.05$).

7.3. Large strain motion of an octant-sphere

In the last example an octant of a sphere is divided into two parts, which are independently meshed. This leads to a highly curved and non-conforming interface, similar in design to the pressurized sphere in Puso [16, Chapter 5.2]. Figure 17 shows the reference configuration of the two parts. The outer part consists of 224 elements, distributed in the following way: four elements through the thickness and $9 \times 9 \times 8$ elements along the edges. The inner part consists of 832 elements, four elements through the thickness and $17 \times 17 \times 16$ elements along the edges. The outer radius of the octant-sphere is 1.2, the inner radius is 1.0, and the interface is located at a radius of 1.1. The material model and parameters correspond to the one chosen in Section 7.1 for the large strain example. Furthermore, an external pressure load using the same characteristics as in Section 7.1 with a maximum pressure of $p = 350$ has been applied to the outer surface. In Figure 18 a sequence of deformed configurations at $t = 0, 1.66, 3.33, 5$ is displayed. For $t > 0.5$, no external forces are acting so that the system under consideration can be classified as Hamiltonian system with symmetries. The evolution of the total angular momentum is depicted in Figure 19. In addition to that, Figures 20 and 21 show the total linear momentum and the total energy, respectively. As expected, these quantities are conserved up to numerical round-off, regardless of the time step size employed.

8. CONCLUSIONS

We have presented a reformulation of the mortar mesh-tying constraints, which yields frame-indifference without changing the initial finite element meshes. To make possible the design of an energy–momentum scheme, a specific coordinate augmentation technique has been developed. The numerical examples deal with three-dimensional large-deformation domain decomposition problems and confirm the enhanced numerical stability and robustness of the newly developed method.

DOI: 10.1002/nme

Owing to the fact that the proposed form of the mortar constraints relies on the decomposition in normal and tangential components, the present approach is well-suited for the application to three-dimensional large-deformation contact problems.

REFERENCES

1. Quarteroni A, Valli A. *Domain Decomposition Methods for Partial Differential Equations*. Oxford Science Publications: Oxford, 1999.
2. Schwarz HA. Über einen Grenzübergang durch alternierendes verfahren. *Vierteljahrsschrift der Naturforschenden Gesellschaft in Zürich* 1870; **15**:272–286.
3. Hackbusch W. *Multi-Grid Methods and Applications*. Springer: Berlin, 1985.
4. Wohlmuth BI. *Discretization Methods and Iterative Solvers Based on Domain Decomposition*. Springer: Berlin, 2000.
5. Widlund OB, Keyes DE (eds). *Domain Decomposition Methods in Science and Engineering*, vol. XVI. Lecture Notes in Computational Science and Engineering, vol. 55. Springer: Berlin, 2006.
6. Widlund OB, Keyes DE (eds). *Domain Decomposition Methods in Science and Engineering*, vol. XVII. Lecture Notes in Computational Science and Engineering, vol. 60. Springer: Berlin, 2008.
7. Hallquist JO, Goudreau GL, Benson DJ. Sliding interfaces with contact-impact in large-scale Lagrangian computations. *Computer Methods in Applied Mechanics and Engineering* 1985; **51**:107–137.
8. Laursen TA. *Computational Contact and Impact Mechanics*. Springer: Berlin, 2002.
9. Wriggers P. *Computational Contact Mechanics* (2nd edn). Springer: Berlin, 2006.
10. El-Abbasi N, Bathe KJ. Stability and patch test performance of contact discretizations and a new solution algorithm. *International Journal for Numerical Methods in Engineering* 2001; **79**:1473–1486.
11. Bernardi C, Mayday Y, Patera AT. Domain decomposition by the mortar method. In *Asymptotic and Numerical Methods for Partial Differential Equations with Critical Parameters*, Kaper H *et al.* (eds). Kluwer Academic Publishers: Dordrecht, The Netherlands, 1993; 269–286.
12. Bernardi C, Mayday Y, Patera AT. A new nonconforming approch to domain decomposition: the mortar element method. In *Nonlinear Partial Differential Equations and their Applications*, Brezis H, Lions JL (eds). Longman Scientific & Technical: Harlow, U.K., 1994; 13–51.
13. Krause R, Wohlmuth BI. Nonconforming domain decomposition techniques for linear elasticity. *East–West Journal of Numerical Mathematics* 2000; **8**(3):177–206.
14. Dohrmann CR, Key SW, Heinstein MW. Methods for connecting dissimilar three-dimensional finite element meshes. *International Journal for Numerical Methods in Engineering* 2000; **47**:1057–1080.
15. Heinstein MW, Laursen TA. A three dimensional surface-to-surface projection algorithm for non-coincident domains. *Communications in Numerical Methods in Engineering* 2003; **19**:421–432.
16. Puso MA. A 3d mortar method for solid mechanics. *International Journal for Numerical Methods in Engineering* 2004; **59**:315–336.
17. Puso MA, Laursen TA, Solberg J. A segment-to-segment mortar contact method for quadratic elements and large deformations. *Computer Methods in Applied Mechanics and Engineering* 2008; **197**:555–566.
18. Yang B, Laursen TA, Meng X. Two dimensional mortar contact methods for large deformation frictional sliding. *International Journal for Numerical Methods in Engineering* 2005; **62**:1183–1225.
19. Yang B, Laursen TA. A contact searching algorithm including bounding volume trees applied to finite sliding mortar formulation. *Computational Mechanics* 2008; **41**:189–205.
20. Hesch C, Betsch P. A comparison of computational methods for large deformation contact problems of flexible bodies. *Zeitschrift für Angewandte Mathematik und Mechanik* 2006; **86**:818–827.
21. Gonzalez O. Time integration and discrete Hamiltonian systems. *Journal of Nonlinear Science* 1996; **6**:449–467.
22. Gonzalez O. Mechanical systems subject to holonomic constraints: differential–algebraic formulations and conservative integration. *Physica D* 1999; **132**:165–174.
23. Betsch P, Steinmann P. Conserving properties of a time FE method—Part II: time-stepping schemes for non-linear elastodynamics. *International Journal for Numerical Methods in Engineering* 2001; **50**:1931–1955.
24. Betsch P, Steinmann P. Conservation properties of a time FE method. Part III: mechanical systems with holonomic constraints. *International Journal for Numerical Methods in Engineering* 2002; **53**:2271–2304.
25. Armero F, Romero I. On the formulation of high-frequency dissipative time-stepping algorithms for nonlinear dynamics. Part I: low-order methods for two model problems and nonlinear elastodynamics. *Computer Methods in Applied Mechanics and Engineering* 2001; **190**:2603–2649.

DOI: 10.1002/nme

26. Armero F, Romero I. On the formulation of high-frequency dissipative time-stepping algorithms for nonlinear dynamics. Part II: second-order methods. *Computer Methods in Applied Mechanics and Engineering* 2001; **190**:6783–6824.
27. Laursen TA, Chawla V. Design of energy conserving algorithms for frictionless dynamic contact problems. *International Journal for Numerical Methods in Engineering* 1997; **40**:863–886.
28. Armero F, Petöcz E. Formulation and analysis of conserving algorithms for frictionless dynamic contact/impact problems. *Computer Methods in Applied Mechanics and Engineering* 1998; **158**:269–300.
29. Laursen TA, Love GR. Improved implicit integrators for transient impact problems—geometric admissibility within the conserving framework. *International Journal for Numerical Methods in Engineering* 2002; **53**:245–274.
30. Hauret P, Le Tallec P. Energy-controlling time integration methods for nonlinear elastodynamics and low-velocity impact. *Computer Methods in Applied Mechanics and Engineering* 2006; **195**:4890–4916.
31. Haikal G, Hjelmstad KD. A finite element formulation of non-smooth contact based on oriented volumes for quadrilateral and hexahedral elements. *Computer Methods in Applied Mechanics and Engineering* 2007; **196**:4690–4711.
32. Betsch P, Hesch C. Energy–momentum conserving schemes for frictionless dynamic contact problems. Part I: NTS method. In *IUTAM Symposium on Computational Methods in Contact Mechanics*, Wriggers P, Nackenhorst U (eds). IUTAM Bookseries, vol. 3. Springer: Berlin, 2007; 77–96.
33. Hesch C, Betsch P. A mortar method for energy–momentum conserving schemes in frictionless dynamic contact problems. *International Journal for Numerical Methods in Engineering* 2009; **77**:1468–1500.
34. Hughes TJR. *The Finite Element Method*. Dover: New York, 2000.
35. Truesdell C, Noll W. *The Non-Linear Field Theories of Mechanics* (3rd edn). Springer: Berlin, 2004.
36. Antman SS. *Nonlinear Problems of Elasticity* (2nd edn). Springer: Berlin, 2005.
37. Betsch P, Uhlar S. Energy–momentum conserving integration of multibody dynamics. *Multibody System Dynamics* 2007; **17**(4):243–289.
38. Simo JC, Wriggers P, Taylor RL. A perturbed lagrangian formulation for the finite element solution of contact problems. *Computer Methods in Applied Mechanics and Engineering* 1985; **50**:163–180.
39. Hauret P, Le Tallec P. A discontinous stabilized mortar method for general 3D elastic problems. *Computer Methods in Applied Mechanics and Engineering* 2007; **196**:4881–4900.
40. Gonzalez O. Exact energy and momentum conserving algorithms for general models in nonlinear elasticity. *Computer Methods in Applied Mechanics and Engineering* 2000; **190**:1763–1783.

DOI: 10.1002/nme